Available online at www.sciencedirect.com
SCIENCE DIRECT
Journal of Solid State Chemistry 179 (2006) 753–774
JOURNAL OF SOLID STATE CHEMISTRY
www.elsevier.com/locate/jssc

The structure and ordering of ε-MnO_2

Chang-Hoon Kim[a,1], Zentaro Akase[a,2], Lichun Zhang[a,3], Arthur H. Heuer[a,*], Aron E. Newman[b], Paula J. Hughes[c]

[a]*Department of Materials Science and Engineering, Case Western Reserve University, 10900 Euclid Avenue, Cleveland, OH 44106-7204, USA*
[b]*Physical Sciences Inc., 20 New England Business Center, Andover, MA 01810, USA*
[c]*Energizer Battery Manufacturing, 25225 Detroit Rd., Westlake, OH 44145, USA*

Received 2 August 2005; received in revised form 28 November 2005; accepted 28 November 2005
Available online 23 January 2006

Abstract

The presence of ε-MnO_2 as a major component of electrolytic manganese dioxide (EMD) has been demonstrated by a combined X-ray diffraction/transmission electron microscopy (TEM) study. ε-MnO_2 usually has a partially ordered defect NiAs structure containing 50% cation vacancies; these vacancies can be fully ordered by a low temperature (200 °C) heat treatment to form a pseudohexagonal but monoclinic superlattice.

Numerous fine-scale anti-phase domain boundaries are present in ordered ε-MnO_2 and cause extensive peak broadening and a massive shift of a very intense, 0.37 nm superlattice peak. This suggests a radically different explanation of the ubiquitous, very broad ~0.42 nm peak (~21–22° 2θ, Cu*K*α radiation) in EMDs, which heretofore has been attributed to Ramsdellite containing numerous planar defects. This work confirms the multi-phase model of equiaxed EMDs proposed by Heuer et al. [ITE Lett. 1(6) (2000) B50; Proc. Seventh Int. Symp. Adv. Phys. Fields 92 (2001)], rather than the defective single-phase model of Chabre and Pannetier [Prog. Solid State Chem. 23 (1995) 1] and Bowden et al. [ITE Lett. 4(1) (2003) B1].
© 2005 Elsevier Inc. All rights reserved.

Keywords: Manganese dioxide; X-ray diffraction; Transmission electron microscopy; Alkaline batteries

1. Introduction

The MnO_2/Zn couple is the basis of the widely used Leclanché and alkaline primary batteries. The electrochemically active form of MnO_2 in these batteries is known as electrolytic manganese dioxide (EMD), referring to its method of formation (electrodeposition from a very acidic $MnSO_4$ (or other Mn salt) bath at ~95 °C) and is often referred to as γ-MnO_2. The nomenclature of what constitutes γ-MnO_2 is not crisp, as described below, but it is commonly thought of as an intergrowth of pyrolusite in a Ramsdellite phase with varying degrees of microtwinning [1]. Pyrolusite, also known as β-MnO_2, is the stable form of MnO_2 at ambient conditions and has the tetragonal rutile structure. Ramsdellite has orthorhombic symmetry and has greater electrochemical activity than pyrolusite. ε-MnO_2 is a polymorph with hexagonal symmetry, which has similar electrochemical activity to the so-called γ-MnO_2, and is the focus of much of this paper.

Electrochemists and solid-state chemists usually describe the structure of these MnO_2 polymorphs as involving various packing of [MnO_6] octahedra with different motifs of edge and corner sharing (see [1,2] for comprehensive reviews). Conventional wisdom in the EMD community invokes the "2 × 1 (empty) tunnels" present in polyhedra-based crystal models of Ramsdellite to explain the enhanced electrochemical activity of Ramsdellite compared to pyrolusite, which only contains "1 × 1 tunnels"; in this view, proton transport during electrochemical discharge occurs much more readily within the 2 × 1 tunnels of Ramsdellite than in the 1 × 1 tunnels of pyrolusite. Recent

*Corresponding author. Fax: +1 216 368 8932.
E-mail address: heuer@case.edu (A.H. Heuer).
[1]Present address: Samsung Electro-Mechanics Co., Suwon, Korea.
[2]Present address: Institute of Multdisciplinary Research for Advanced Materials, Tohoku University, Sendai, Japan.
[3]Present address: Department of Metallurgy & Materials Engineering, University of Connecticut, Storrs, CT, USA.

0022-4596/$ - see front matter © 2005 Elsevier Inc. All rights reserved.
doi:10.1016/j.jssc.2005.11.042

theoretical studies by Balachandran et al. [3] suggested, however, that proton transport was faster in Ramsdellite, not due to tunnel size per se, but due to the relative arrangements of oxygen and manganese atoms within the tunnels.

Although we believe that hexagonal ε-MnO_2 may be present in many commercial EMDs (see below), only modest discussion of its electrochemical activity can be found in the literature [1,4–8]. ε-MnO_2 has been reported to form as fibrous electrodeposits [9,10], to form at high current densities [5,6], and to form from $MnCl_2$, $Mn(NO_3)_2$, and $Mn(ClO_4)_2$ solutions [10].

In the original structure determinations of ε-MnO_2, a hexagonal unit cell was proposed, with $a = 0.280$ nm, $c = 0.445$ nm, and space group $P6_3/mmc$ [11]. This proposed structure involves a NiAs-type unit cell, with Mn^{4+} cations randomly occupying 50% of the octahedral positions of the hexagonal-close-packed (hcp) oxygen sublattice, although one-dimensional ordering—Mn^{4+} ion, cation vacancy, Mn^{4+} ion, cation vacancy, etc.—was believed to be present along the *c*-axis. However, ionic compounds of either MO or MO_2 stoichiometry do not usually crystallize in the NiAs structure because the short cation–cation distances give rise to large Coulombic repulsions, although this will be partially ameliorated by the one-dimensional ordering just mentioned.

EMDs usually display powder X-ray diffraction (XRD) patterns containing five rather broad peaks at *d* spacings of ~0.42, 0.242, 0.213, 0.164, and 0.140 nm, with the ~0.42 nm peak being much broader than the others [1,4–10,12–15]. The 0.140 nm peak arises from the $\{11\bar{2}0\}$ planes of ε-MnO_2 (Table 1) and should confirm the presence of this polytype in EMD. However, because of fine particle peak broadening, the 0.242, 0.213, and 0.164 nm peaks could be attributed to any of the three MnO_2 polymorphs (Table 1).

The peak at ~0.42 nm cannot be indexed using the proposed hexagonal unit cell of ε-MnO_2 [1], although JCPDS card no. 30-0820 shows a very weak unidentified peak at a *d* spacing of 0.422 nm (Table 1). There is an intense peak in Ramsdellite close to this *d* spacing (actually 0.4057 nm), but the significant width of this peak in XRD powder patterns has been a subject of much discussion in the literature [1]. As noted already, materials containing this very broad peak are often referred to as γ-MnO_2.

Two defect types within Ramsdellite have been postulated to explain the broad and diffuse nature of the ~0.42 nm XRD peak. De Wolff [16] suggested that EMDs contain disordered intergrowths of Ramsdellite and pyrolusite (the so-called De Wolff defects), which give rise to extensive diffuse X-ray scattering. Chabre and Pannetier [1] further suggested extensive microtwinning in EMDs, and calculated (using the XRD simulation program DIFFaX) the size and spacing of the postulated Ramsdellite and pyrolusite slabs and the extent of microtwinning in a

Table 1
Crystallographic data for MnO_2 polymorphs

Phase	Unit cell parameters	Selected X-ray data		
		d spacing (nm)	*hkl*; *hkil*	Peak intensity
Ramsdellite (JCPDS card no. 43-1455)	Space group *Pbnm*[a]	0.4057	1 1 0	100
	$a = 0.45128$ nm	0.2549	1 3 0	38
	$b = 0.92660$ nm	0.2434	0 2 1	29
	$c = 0.28607$ nm	0.2338	1 1 1	31
		0.2142	1 2 1	19
		0.1903	1 3 1	15
		0.1655	2 2 1	20
		0.1616	2 4 0	12
		0.1471	1 5 1	11
		0.1431	0 0 2	10
Pyrolusite (JCPDS card no. 81-2261)	Space group $P4_2/mnm$	0.3114	1 1 0	100
	$a = 0.44041$ nm	0.2408	1 0 1	52
	$c = 0.28765$ nm	0.2202	2 0 0	9
		0.2113	1 1 1	13
		0.1625	2 1 1	48
		0.1438	0 0 2	6
		0.1308	3 0 1	15
ε-MnO_2 (JCPDS card no. 30-0820)	Space group $P6_3/mmc$	0.422	?	1
	$a = 0.280$ nm	0.242	$1\,0\,\bar{1}\,0$	65
	$c = 0.445$ nm	0.222	0 0 0 2	2
		0.213	$1\,0\,\bar{1}\,1$	35
		0.164	$1\,0\,\bar{1}\,2$	100
		0.140	$1\,1\,\bar{2}\,0$	40

[a]Following Ref. [1] and other literature, we have transformed unit cell parameters as follows from the JCPDS file: $a \rightarrow b$; $b \rightarrow c$; $c \rightarrow a$.

number of EMDs. Their view is that all EMDs are single-phase materials based on a defective Ramsdellite structure and contain De Wolff defects and microtwins.

Bowden et al. [4] took an alternative approach, and also based on a single-phase defective Ramsdellite model. They considered EMD as a homogeneous Ramsdellite structure distorted by one-dimensional chain or ribbon-like pyrolusite defects, and claimed that this approach successfully reproduced XRD patterns of numerous EMDs.

In our previous work [17,18], ε-MnO_2 (also known as the mineral akhtenskite) was confirmed as an independent phase existing in a conventional EMD material, and we showed that the commercial EMD we studied was multi-phase and contained Ramsdellite, ε-MnO_2, and pyrolusite. Structure at two length scales—single-phase nanometer-scale ellipsoidal crystallites making up multi-phase nano-porous submicron "grains"—and evidence of ordering in ε-MnO_2 was found using transmission electron microscopy (TEM).

Simon et al. [19] also advocated a multi-phase model for EMD and performed Rietveld XRD analysis of 24 EMD samples. They assumed that their EMDs (which encompassed samples with BET surface areas ranging from 10 to 86 m^2/gm) contained a mixture of ε-MnO_2, "γ-MnO_2"—essentially the defective Ramsdellite modeled by Chabre and Pannetier [1]—and pyrolusite, and refined lattice parameters and crystallite size of each phase. Most recently, Balachandran et al. [3] performed a first principles study of the structure of stoichiometric and Mn-deficient MnO_2. Standard ferromagnetic spin polarization computations suggested that the vacancy-ordered form of ε-MnO_2 postulated earlier by Heuer et al. [17,18] was lower in energy than both pyrolusite and Ramsdellite, but a correction for paramagnetic disorder confirmed pyrolusite as the ground state of stoichiometric MnO_2.

Ruetschi [20] in 1984 proposed a cation-vacancy model for MnO_2 prepared by electrodeposition. The model assumes that the oxygen sublattice is complete (although some OH^- ions substitute for oxygen for charge compensation) and that vacancies occur only on the manganese sublattice. The two types of cation defects that were proposed are (1) a change of the oxidation state from Mn^{4+} to Mn^{3+} and (2) a manganese cation vacancy. Protons associated with the first defect type are called Coleman protons, while protons associated with the second are called Ruetschi protons.

The chemical formula for the Ruetschi model of manganese dioxide is as follows:

$$Mn^{4+}_{1-x-y}Mn^{3+}_{y}V_{Mn\,x}O_{2-4x-y}(OH)_{4x+y}. \quad (1)$$

Here, V_{Mn} represents the vacancy on the cation sublattice, x is the Ruetschi defect concentration, and y is the Coleman defect concentration [20]. The presence of such Ruetschi defects significantly changes the relative energetics of the various MnO_2 polymorphs [3].

In the present work, a number of bulk EMD materials, including a phase-pure ε-MnO_2, were comprehensively investigated by XRD and TEM to fully understand their phase chemistry and microstructures. The multi-phase nature of some equiaxed (non-fibrous) EMDs and vacancy ordering of ε-MnO_2 have been confirmed, and structure models for two different ordered structures based on ε-MnO_2 are proposed. Significantly, one of these ordered phases of ε-MnO_2 has its strongest XRD peak at a d spacing of 0.37 nm. We suggest that planar defects—anti-phase domain boundaries (APBs)—within this ordered structure cause this "superlattice" peak to be broadened and shifted to apparently larger d spacings; this type of peak shift does not occur for the "fundamental" peaks common to ordered and disordered ε-MnO_2. In essence, we suggest a new origin for the ~0.42 nm XRD peak that is present in many commercial EMDs. Finally, if the term "γ-MnO_2" is retained by the EMD community, we recommend it be used to refer to materials absent the characteristic 0.140 nm peak of ε-MnO_2 and with the anomalous peak having a d spacing of 0.395 nm or smaller (2θ of 22.5° or larger, Cu$K\alpha$ radiation).

2. Experimental procedure

Of the many EMDs we studied, particular focus was given to three materials: a sample of production EMD described in our earlier work [17,18] (henceforth sample I); a laboratory EMD sample provided by Dr. P. Slezak of Energizer Battery Manufacturing (henceforth sample II); and a laboratory EMD sample provided by Dr. O. Schilling of Erachem Comilog (henceforth sample III). As far as is known, all samples had been electrodeposited from very acidic $MnSO_4$ solutions at temperatures near 95 °C. All samples were available as bulk (chip) specimens, and as powders ground from a portion of the chips in the conventional manner.

XRD patterns of both types of specimens were recorded; experiments at Case Western Reserve University used a Scintag X-1 XRD θ–θ instrument, with Cu$K\alpha$ radiation in the 2θ range 15–70° and a scanning rate of 0.1°/min; experiments at Energizer Battery Manufacturing used a Brucker D8 instrument with a wide area detector, a similar scanning rate, and Cr$K\alpha$ radiation (these latter XRD patterns have been reformatted to appear in this paper as if they had been generated with Cu$K\alpha$ radiation). For convenience, we refer to various peaks either by their d spacings or their 2θ angles for Cu$K\alpha$ radiation.

Following earlier work [19], we attempted Rietveld analysis on the powder XRD patterns of all three specimens. (The Rietveld analysis is briefly described in Appendix A.) We used a program in the public domain [21] and refined the data, assuming that each powder was a mixture of the three most common MnO_2 polymorphs, pyrolusite, Ramsdellite, and ε-MnO_2. As input to the analysis, we used the lattice parameters for these phases shown in Table 1.

It is emphasized that we performed this analysis solely to provide a comparison with prior literature, e.g., Refs. [1,19], in which XRD was the primary diffraction tool used for phase identification. As the subsequent TEM-based analysis will show, XRD alone cannot provide unambiguous phase identification of EMDs.

Electron transparent thin foils were made from the bulk specimens using the conventional procedure used for ceramics, involving preparation of an ~90 μm thick petrographic section by grinding and polishing with diamond abrasives, "dimpling" to further reduce the thickness of the section, and ion thinning to electron transparency. In some cases, ion-beam-induced radiation damage resulting in radiation-induced phase transformation was observed and is described in Appendix B. We found that use of a liquid N_2-cooled stage for ion-beam thinning significantly limited the extent of the ion-beam-induced damage, and used such a stage for preparing most of the TEM thin foils from which the data discussed in this paper were acquired.

The electron transparent TEM foils were investigated using a Philips CM 20 instrument operating at 200 keV for conventional TEM imaging and diffraction analysis; the electron diffraction patterns were acquired with an ~10 nm diameter electron probe using the microdiffraction mode on the TEM. High-resolution TEM (HREM) imaging was performed using a Technai F-30 FEG-TEM operating at 300 keV.

3. Results and discussion

3.1. Phase analysis of samples I, II, and III

Fig. 1 shows powder XRD pattern of samples I, II, and III, Figs. A.1–A.3 in Appendix A show the Rietveld fits for these three patterns. The powder XRD patterns appear to be very similar, aside from modest peak shifts between the three powders and equally modest changes in the peak breadths. At first sight, the Rietveld analyses (see Figs. A.1–A.3) appear to show that all three samples are "conventional" EMDs, containing roughly comparable amounts of Ramsdellite (44–50%) and ε-MnO_2 (44–51%), with only modest amounts of pyrolusite (5–9%). However, the peaks for sample III in Fig. 1 have been labeled using ε-MnO_2 indices (except for the ~0.42 nm (~21° 2θ) peak), as further analysis (see below) showed this sample to be 100% phase-pure ε-MnO_2.

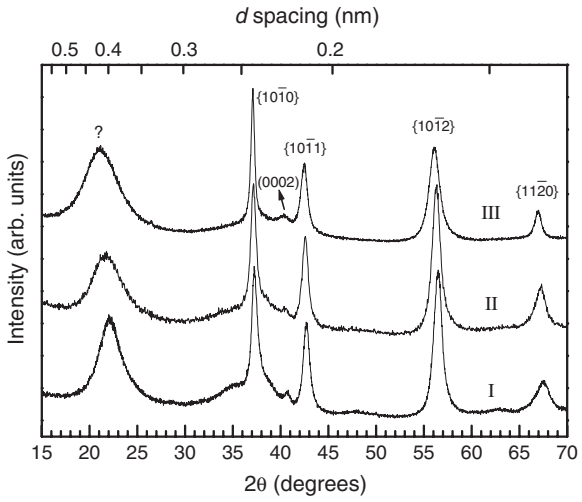

Fig. 1. Powder XRD patterns of EMD samples I, II, and III.

As noted in Appendix A, the Rietveld analysis can in principle yield particle size and strain for each constituent; however, the Rietveld analyses of these EMD powders were unsatisfactory. For example, negative particle sizes were found for ε-MnO_2 in sample I and for pyrolusite in sample II (data not included here), and the magnitude of the statistical parameter ***s*** (see Appendix A) for samples I, II, and III was also rather large (1.87, 1.28, and 1.92, respectively). This problem arises mainly because of the assumption that the broad ~0.42 nm peak arises from defective Ramsdellite, as standard Rietveld analysis has no provision for dealing with defective solids of the type under study here; furthermore it leads to a very fine particle size for this phase in materials, I, II, and III (3, 2, and 2 nm, respectively). Although electron diffraction data relative to these three phases will be shown in Section 3.2, we note here that the Rietveld-phase fraction analysis of sample I is in tolerable agreement with our earlier work on the same material [17], where we concluded, from analysis of 64 electron microdiffraction patterns, that sample I contained ~50% Ramsdellite, ~35% ε-MnO_2, and ~10% pyrolusite. A more recent analysis from a newly prepared TEM foil confirmed the Ramsdellite-rich nature of sample I; of 11 microdiffraction patterns recorded, nine (82%) were from Ramsdellite, and two (18%) from ε-MnO_2.

A similar analysis of 79 single-phase microdiffraction patterns from sample II revealed that 58 (73%) were from ordered ε-MnO_2 (see Section 3.3) and 15 (19%) were from Ramsdellite; the remaining six (8%) could not be solved.[4] This analysis seriously contradicts the Rietveld-phase chemistry determination for sample II (see Fig. A.2). In this regard, it is relevant to note that the XRD analysis samples a volume of material many orders of magnitude larger than is available in a TEM foil, and whether a particular TEM foil is representative of the bulk material is always a worry. Nevertheless, the negative particle sizes noted above and the discrepancies between the Rietveld powder X-ray determination and the TEM determination of phase chemistry to be discussed below are striking. (Actually, Chabre and Pannetier [1] cautioned that the high density of lattice defects in their model of "γ-MnO_2" precluded the use of traditional crystallographic techniques such as the Rietveld profile refinement.)

[4]We believe that these unsolved diffraction patterns were from one of these phases in a high-order zone-axis orientation, or were from one of the rarer MnO_2 polymorphs. We also recorded a small number of unsolvable diffraction patterns of sample I.

A final and most serious problem is that analysis of more than a hundred electron microdiffraction patterns of sample III revealed that all were from ε-MnO_2! If the TEM data for samples II and III are any indication, a good deal of the prior XRD literature on EMDs must be viewed with caution.

The significant concern with the traditional XRD powder approach was reinforced by the XRD patterns of the bulk specimen of sample III. As was reported previously [17], the XRD pattern from the chip of sample I available to us was independent of the orientation of the chip relative to the electrodeposition geometry, and was similar to the powder XRD pattern of the same material. The same was true for sample II.

Sample III was quite different, in that there are major differences between the top surface and cross-sectional XRD patterns (Fig. 2). As indicated by the labeling of the XRD peaks, the sample appears to be strongly textured, and is essentially phase-pure ε-MnO_2 (again disregarding for now the broad 0.417 nm (21.3° 2θ) peak). In particular, the top surface spectrum shows a very strong $\langle 11\bar{2}0\rangle$ texture. A bulk XRD spectrum very similar to Fig. 2 has been reported previously in a fibrous EMD by Preisler [10]. The difference between the powder XRD pattern of sample III, which suggests a conventional multi-phase EMD ("γ-MnO_2"), and the bulk XRD patterns of Fig. 2, which suggests a textured 100% phase-pure ε-MnO_2, shows the dangers of relying on XRD powder patterns for phase characterization of EMDs.

For reasons related to our earlier suggestion [17,18] of the possibility of vacancy ordering in ε-MnO_2 (assuming the structure to be a NiAs-type with 50% of the cation sites vacant), we heat-treated samples of the 100% ε-MnO_2 sample III in air for various times at 100, 200, and 300 °C. The powder XRD spectrum of material heat treated at 200 °C for 198 h, Fig. 3, reveals peak shifts to smaller *d* spacings (larger 2θ angles), as well as some peak broadening of the "fundamental" reflections, $\{10\bar{1}0\}$, (0002), $\{10\bar{1}1\}$, $\{10\bar{1}2\}$, and $\{11\bar{2}0\}$; however, the anomalous 0.417 nm peak has shifted by nearly 2° 2θ to a *d* spacing of 0.384 nm (23.2° 2θ), and a new minor peak has appeared at a *d* spacing of 0.268 nm (33.5° 2θ). The longest anneal we performed was of 198 h at 200 °C and we note that samples heat treated at 100 °C or for shorter times at 200 °C gave similar XRD patterns (data not included here), but the peak shifts and changes in peak breadth were smaller. This clearly suggests that kinetic factors are involved in these structural changes, but these have not been studied in detail.

Considering only the fundamental reflections, the peak positions in the 198 h sample suggest significant lattice "shrinkage"; analysis of the fundamental peaks showed that the *c* and *a* parameters changed from 0.4453 and 0.2792 nm in the as-received powder sample ($c/a = 1.595$), in reasonably good agreement with JCPDS data (Table 1), to 0.4385 and 0.2760 nm ($c/a = 1.589$) in the 198 h/200 °C sample, indicating a volume shrinkage of 3.8% ($\Delta c = 1.5\%$ and $\Delta a = 1.1\%$).

Fig. 3 also shows the XRD pattern of a powder sample heat treated for 30 min at 300 °C. Quite different changes have occurred. The ~0.417 nm peak has been replaced by a peak with a *d* spacing of 0.356 nm (25.0° 2θ), a new peak corresponding to a *d* spacing of 0.290 nm (30.8° 2θ) has appeared, the fundamental $\{10\bar{1}0\}$, $\{10\bar{1}1\}$, and $\{10\bar{1}2\}$ peaks have undergone peak shifts less marked than those observed at 200 °C, and the $\{11\bar{2}0\}$ peak, which is at a *d* spacing of 0.138 nm (67.9° 2θ) in the 200 °C sample, has split and is replaced by peaks at *d* spacings of 0.140 nm (66.8° 2θ) and 0.136 nm (69.0° 2θ). This latter change suggests that hexagonal symmetry may have been lost by the 300 °C heat treatment.

As a matter of interest, we applied Chabre and Pannetier's [1] classification scheme to the powder XRD patterns shown in Fig. 1. All three samples are Type III

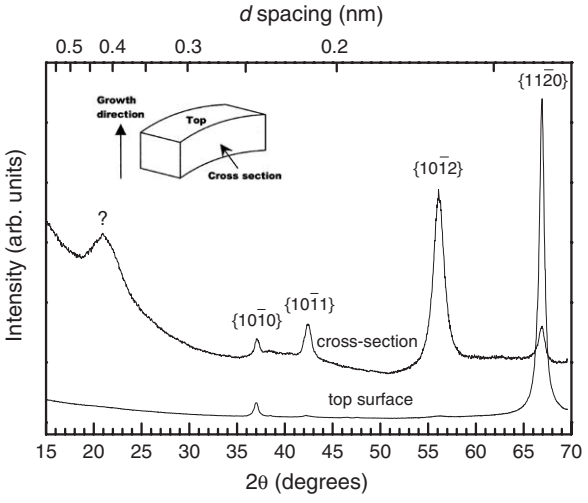

Fig. 2. Bulk XRD patterns of two orthogonal scans of sample III. The schematic drawing shows the geometry of the bulk chip.

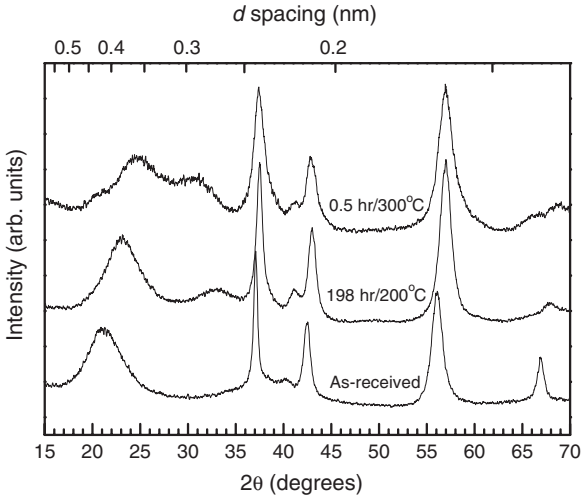

Fig. 3. Powder XRD patterns of sample III as-received, after heat treatment for 198 h at 200 °C, and after 0.5 h at 300 °C.

material, i.e., the extent of microtwinning is 100%. The P_r number—the fraction of pyrolusite in the supposed De Wolff defects—is 0.36 for sample I, 0.26 for sample II, and 0.02 for sample III. However, it will be made clear in Section 4 that we do not believe that Chabre and Pannetier's defect model for EMDs is applicable to any of our materials.

3.2. TEM studies

3.2.1. Microstructure

Fig. 4 is a conventional bright-field transmission electron micrograph showing a typical area of sample I; it is, to all intents and purposes, identical to the microstructures of sample II and to a number of other EMDs not discussed in this paper. Structure is present at two length scales, nanoporous equiaxed "grains", 0.1–0.2 μm in diameter, and ellipsoidal crystallites, ~10–30 nm in characteristic dimension (inset in Fig. 4). This type of EMD microstructure was described previously for sample I [17,18]; it obviously reflects conditions at the electrodeposit/bath interface during production of EMD, but detailed discussion of the genesis of EMD microstructures is beyond the scope of this work. Significantly, no defects that could be attributed to De Wolff disorder or microtwinning were visible in any of the TEM micrographs we recorded.

Fig. 5 shows the microstructure of sample III; it is clearly very different. Fig. 5a is an image taken from a cross-sectional foil of the as-received material; the microstructure is fibrous, the fibers being >1 μm long, with aspect ratios much greater than 10. The cross-sectional images from the heat-treated sample were essentially the same.

Plan view images from orthogonal sections (i.e., foils prepared parallel to the top surface) of the as-received and 200 °C heat-treated samples were also similar; an example from a heat-treated sample is shown in Fig. 5b. Structure is also present at two length scales, the micron-long fibers and the ~10–50 nm ellipsoidal crystallites making up the fiber cross section. The fibers are approximately rectangular in cross section, with an aspect ratio of 3–10. Each fiber (or more accurately each lathe) contains stacks of similarly oriented crystallites, whose characteristic thickness, ~15 nm, could be obtained from the width of the $\{11\bar{2}0\}$ peak in the bulk XRD pattern of as-received sample III shown in Fig. 2. A schematic drawing of the fibers is shown in Fig. 5c. Contrary to the XRD data, there was no change in the lathe/crystallite microstructure during the low temperature heat treatments.

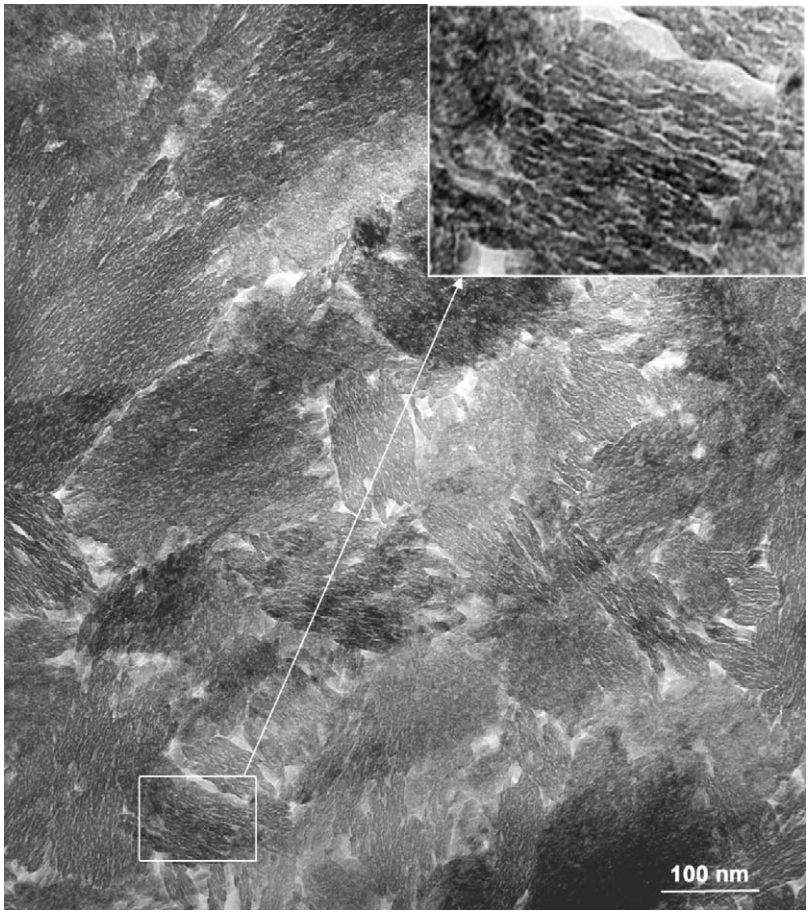

Fig. 4. Bright-field TEM image of typical microstructure of sample I.

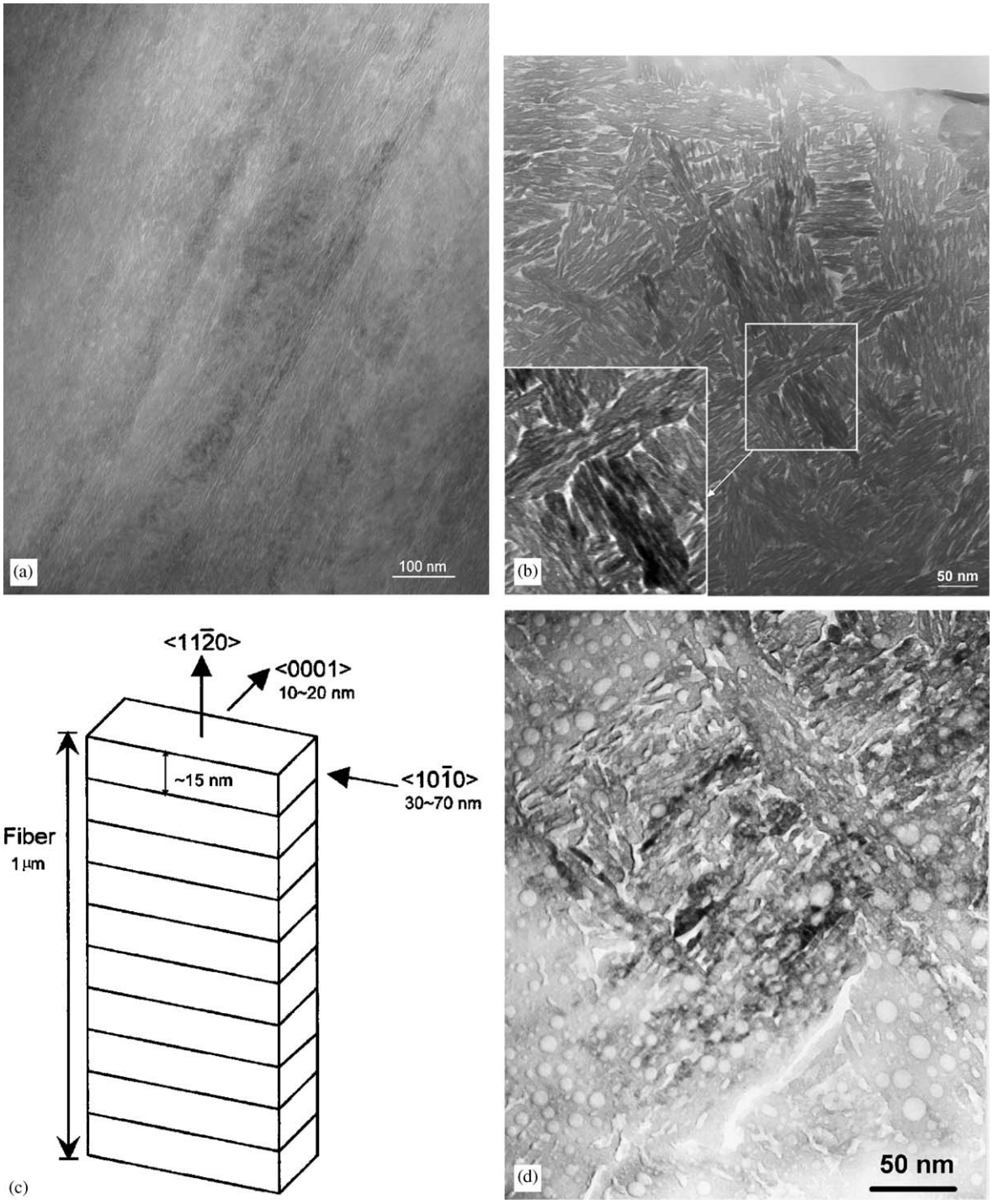

Fig. 5. Bright-field TEM image: (a) shows the microstructure in a cross-sectional foil of sample III as-received; (b) shows the microstructure in a plan view foil after the 1 h/200 °C heat treatment; and (d) shows the microstructure in a plan view foil after the 0.5 h/300 °C heat treatment. (c) is a schematic drawing of the fiber geometry. See text for further discussion.

The situation with regard to the 300 °C heat treatment is very different. A plan view image is shown in Fig. 5d. The lath-like microstructure is present but is obscured by prominent new features in the form of light-colored disk-shaped regions, which subsequent electron diffraction analysis (see below) suggests is evidence for a new ordered structure.

3.2.2. *Microcrystallography*

A selection of labeled microdiffraction patterns of Ramsdellite crystallites is shown in Fig. 6, while comparable data for ε-MnO_2 are shown in Fig. 7. We show this data to emphasize that in the vast majority of cases, it is possible to distinguish these two MnO_2 polymorphs without difficulty in electron microdiffraction patterns.

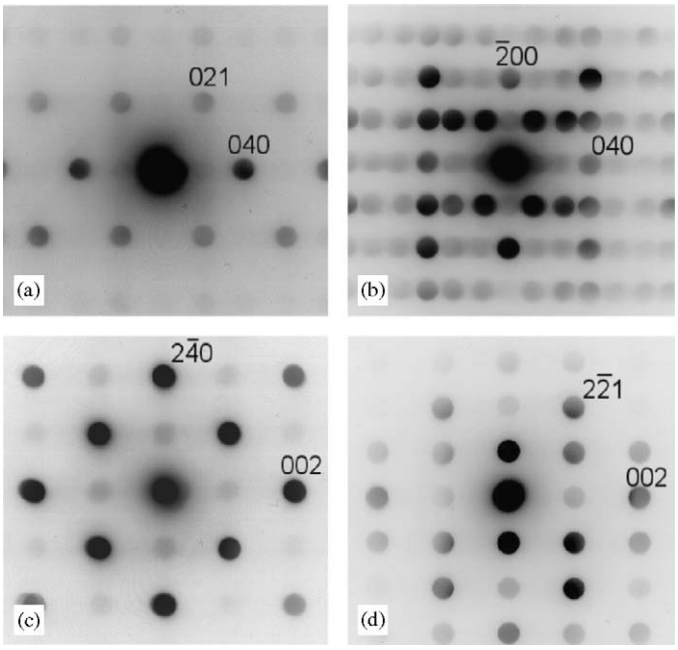

Fig. 6. Ramsdellite electron microdiffraction patterns: (a) ⟨001⟩, (b) ⟨001⟩, (c) ⟨210⟩, and (d) ⟨110⟩ zone-axis orientations.

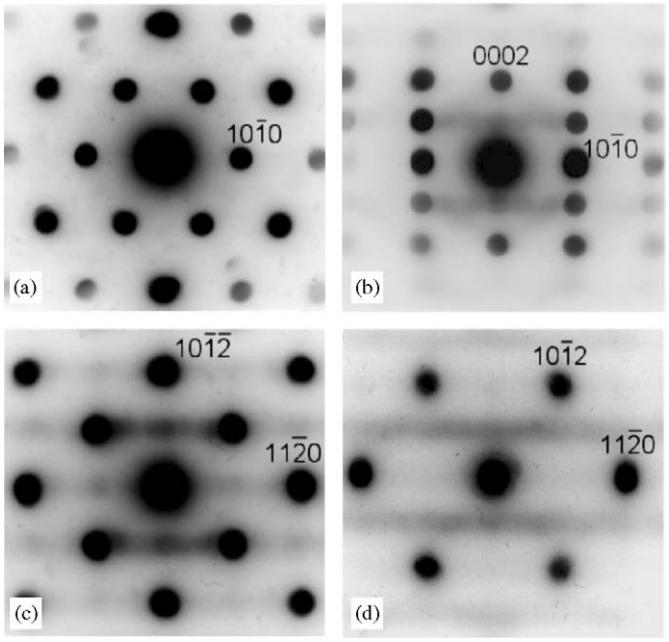

Fig. 7. ε-MnO_2 electron microdiffraction patterns from as-received sample III: (a) ⟨0001⟩, (b) ⟨$11\bar{2}0$⟩, (c) ⟨$01\bar{1}1$⟩, and (d) ⟨$02\bar{2}1$⟩ zone-axis orientations.

This has been discussed in the past by us [17] and others [4], and is discussed further in Appendix C.

Assuming that the TEM foils prepared from samples I, II, and III are representative of the EMD chips, we estimate that the Ramsdellite content of these samples are ~50%, ~25%, and 0%, respectively. As noted already, this is in striking disagreement to the Rietveld XRD analysis shown in Figs. A.1–A.3, which indicates Ramsdellite contents of 44%, 44%, and 50%, respectively; the discrepancies for samples II and III are due entirely to the assumption that the broad ~0.42 nm XRD peak arises from defective Ramsdellite. In this regard, although more than 200 Ramsdellite electron microdiffraction were recorded during the course of this work from samples I and II and from other EMDs, only one example of microtwinning was found.

All the microdiffraction patterns shown in Fig. 7 were taken from specimen III, and confirmed both the phase content (100% ε-MnO_2) and the texture revealed by the cross-sectional XRD pattern (Fig. 2). Thus, *all* microdiffraction patterns obtained from the top surface foils (with microstructures similar to that shown in Fig. 5b) had ⟨$11\bar{2}0$⟩ zone-axis orientations (Fig. 7b), but had a random rotational orientation. The other microdiffraction patterns in Fig. 7 were taken from cross-sectional foils after tilting to the appropriate zone-axis orientation. Diffuse streaking occurs in all zone-axis orientations but ⟨0001⟩ (Fig. 7a).

It is important to note that the evidence for vacancy ordering in ε-MnO_2 reported earlier [17,18] had come from occasional examples of discrete "tripling" reflections (reciprocal lattice **g** vectors 1/3 as long as the "fundamental" reciprocal lattice vectors) in ⟨$11\bar{2}0$⟩ zone-axis patterns in ε-MnO_2 patterns from sample I. In sample III, these discrete "superlattice" reflections are streaked parallel to a ⟨$10\bar{1}0$⟩ direction (see Fig. 7b, for example), while in sample II, these reflections were very sharp, indicating (as will soon be clear) the presence of an ordered form of ε-MnO_2 (see next).

Fig. 8 includes a more extensive set of microdiffraction patterns showing ordering in ε-MnO_2: (a)–(d) are from heat-treated sample III while (e) and (f) are from sample II. The streaking evident in the electron microdiffraction patterns in Fig. 7 has for the most part been replaced by discrete superlattice reflections. These invariably occur at positions 1/3, 2/3, or 1/2[5] of the reciprocal lattice distances between the fundamental reflections; we refer to these as tripling or doubling reflections, respectively. The indexing shown in these patterns (and in Fig. 9 to be discussed next) derives from the structure of the ordered forms of ε-MnO_2 discussed in Section 3.3. It is interesting to note that Charenton and Strobel [22] had previously observed tripling reflections in electron diffraction patterns from "γ-MnO_2" but interpreted them in terms of De Wolff disorder.

The presence of superlattice reflections arising from the 200 °C heat treatment is convincing confirmation that vacancy ordering can occur in ε-MnO_2. Anti-phase domains separated by APBs are a common feature in ordered metallic alloys, and in oxide ceramics and minerals which have undergone various types of phase transforma-

[5]"Forbidden" (0001) reflections were occasionally present, albeit with variable intensity; they occur as a consequence of dynamical electron diffraction effects, i.e., double diffraction.

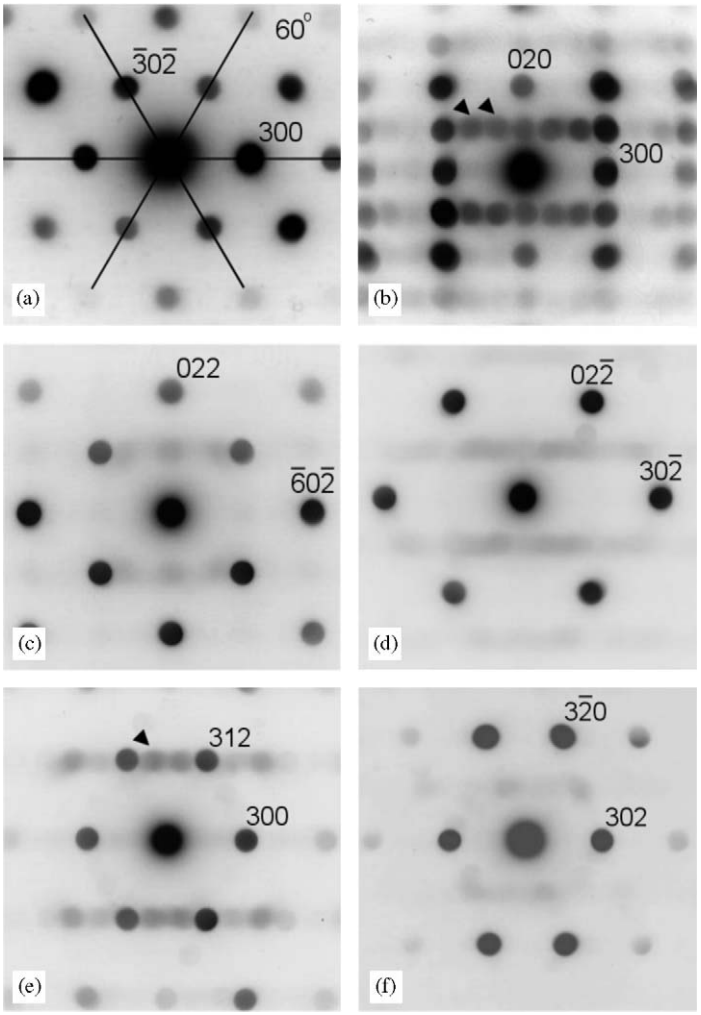

Fig. 8. Ordered ε-MnO_2 electron microdiffraction patterns: (a) ⟨010⟩, (b) ⟨001⟩, (c) ⟨13$\bar{3}$⟩, (d) ⟨233⟩, (e) ⟨0$\bar{2}$1⟩, and (f) ⟨23$\bar{3}$⟩ zone-axis orientations. ε^{vo}-MnO_2 indices. The arrowed reflections in (b) are the "tripling" superlattice reflections. The arrow in (e) points to a (112) reflection. (a)–(d) are from heat-treated sample III, while (e) and (f) are from as-deposited sample II.

tions [23]. They are likely planar defects in ordered ε-MnO_2 as well—in fact, the streaking in the microdiffraction patterns in Fig. 7 is almost certainly a consequence of a very small domain size, i.e., a high density of APBs, as is discussed further below. However, the fine scale of the ε-MnO_2 crystallites present in all our samples makes difficult the traditional, diffraction contrast TEM experiments to study domain microstructures; instead, we resorted to HREM, as will be described in Section 3.2.3.

Not surprisingly, electron microdiffraction patterns from sample III after the 300 °C heat treatment (Fig. 9) show major changes from those found after the 200 °C heat treatment. The "basal" zone has lost six-fold symmetry (Fig. 9a), the superlattice tripling reflections in some ⟨11$\bar{2}$0⟩-derived patterns have assumed incommensurate positions (arrowed in Fig. 9b), while in others, they have maintained their 1/3, 2/3 spacings (arrowed in Fig. 9c), and the doubling superlattice reflections in ⟨01$\bar{1}$1⟩ and ⟨02$\bar{2}$1⟩-derived zone-axis patterns have increased in intensity (arrowed in Figs. 9d and e).

We considered whether Ramsdellite or pyrolusite might have formed during the 300 °C heat treatment but were able to reject this possibility. No electron diffraction patterns suggestive of pyrolusite were found. In the case of Ramsdellite, the zone-axis orientations that are closest to Figs. 9d and e are [21$\bar{6}$] and [210], respectively. Fig. 9d, however, cannot be indexed as Ramsdellite because the Ramsdellite [21$\bar{6}$] zone-axis pattern is asymmetric. Fig. 9e is also a very poor fit to a Ramsdellite [210] orientation, as the interplanar angles do not agree with simulated electron diffraction patterns (this aspect of identifying electron diffraction patterns is discussed in detail in Appendix C). We, thus, conclude that an ordering motif different from that found after the 200° heat treatment, and a "breaking" of the hcp symmetry of the oxygen sublattice, must have occurred at 300 °C.

Images roughly similar to Fig. 5d and incommensurate diffraction spots comparable to those shown in Fig. 9b have been reported in ordered Al–Ti alloys containing between 35% and 43% Al [24]. In such alloys, two ordering

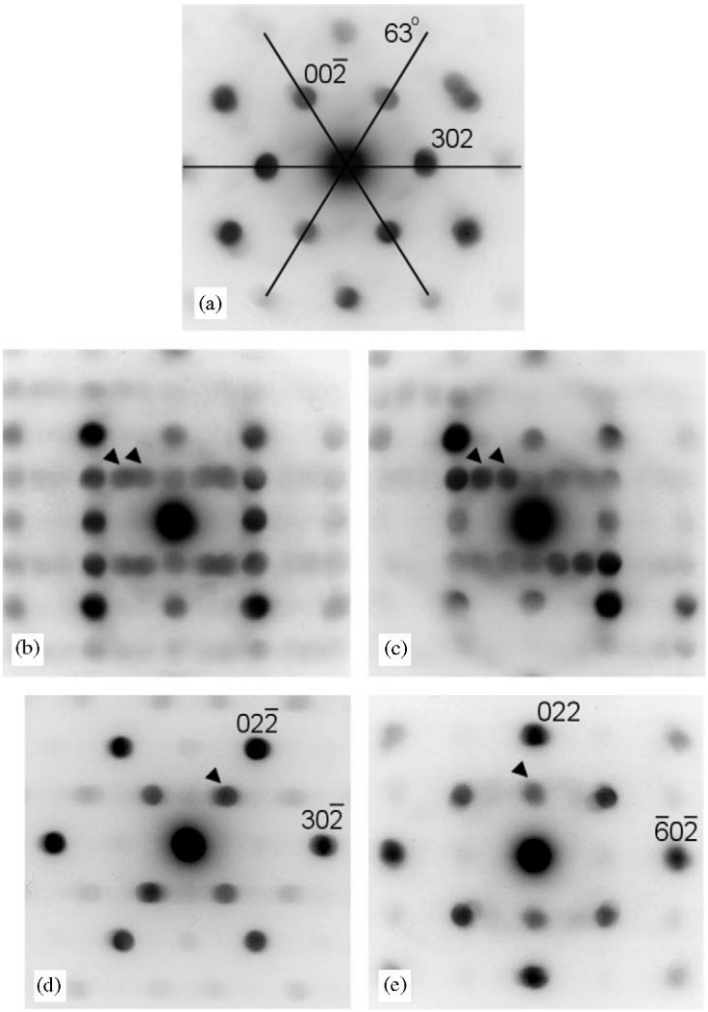

Fig. 9. Electron microdiffraction patterns of sample III after the 0.5 h 300 °C heat treatment: (a) ⟨010⟩, (b) ⟨001⟩, (c) ⟨001⟩, (d) ⟨233⟩, and (e) ⟨13$\bar{3}$⟩ zone-axis orientations. (b) and (c) are the same basic orientation but show incommensurate and commensurate (ε^{vo}-MnO_2-type) superlattice reflections, respectively (the arrowed reflections). The arrowed reflections in (d) and (e) are "doubling" superlattice reflections ε^{bhs}-MnO_2 indices.

motifs are possible, one for Al_5Ti_3 and the other for $Al_{11}Ti_7$, the incommensurate reflections arising from the average structure. The fact that both commensurate and incommensurate reflection are present in different regions of the 300 °C TEM foil indicate that this material is a mixture of the ordered ε-MnO_2 whose diffraction patterns are shown in Fig. 8 and domains of a second-ordered phase, the disk-shaped features in Fig. 5d.

3.2.3. *HREM studies*

Before describing the HREM studies, it is worth remarking that TEM, HREM, and electron diffraction studies of EMD present serious challenges to the electron microscopist. In the first place, while TEM thin foil preparation for the equiaxed samples I and II was relatively straightforward—they were very "ceramic-like"—this was not the case for sample III. In particular, the fibrous microstructure of sample III caused it to be very friable, which made making TEM plan view thin foil specimens, i.e., sections parallel to the top surface, particularly difficult. Secondly, the very small crystallite size made the conventional type of diffraction contrast experiments, which require detailed tilting experiments to confirm phase identification, or for characterization of APB-type planar defects, very difficult to execute, even with the state-of-the-art goniometric tilting stages on our TEM instruments. Finally, there is the occurrence of ion-beam-induced phase transformation, which is discussed in Appendix B. While we resolved this issue for the most part by using a liquid N_2-cooled stage for ion thinning foil preparation, the sensitivity of MnO_2 to such damage renders the thinnest regions of our foils—the regions most suitable for HREM—unusable. Thus, the HREM had to be performed in regions thicker than was ideal. *Caviat emptor*!

Fig. 10 shows an HREM image of a top surface foil, i.e., a foil with a {11$\bar{2}$0} orientation, prepared from the as-received chip of sample III. A fine-scale domain structure, with characteristic dimensions of ~5 to ~10 nm, is present; this domain structure is much finer than the ~30 nm wide by ~70 nm long crystallites visible in Fig. 5b. The domain

boundaries are responsible for the streaking (“rel-rods” in TEM parlance) present in the electron diffraction patterns shown in Figs. 7b–d. (It is well known (see Ref. [25], for example) that two-dimensional (planar) defects in real space, i.e., APBs visible in electron micrographs, will cause intensity perpendicular to the boundaries in reciprocal space, i.e., streaking associated with superlattice reflections in electron diffraction patterns. The normals to the boundaries in real space determine the streak direction in reciprocal space.) We will argue in Section 4 that these APBs and their associated rel-rods are also responsible for the extreme breadth of the ~0.42 nm peak of the XRD powder patterns of Fig. 1.

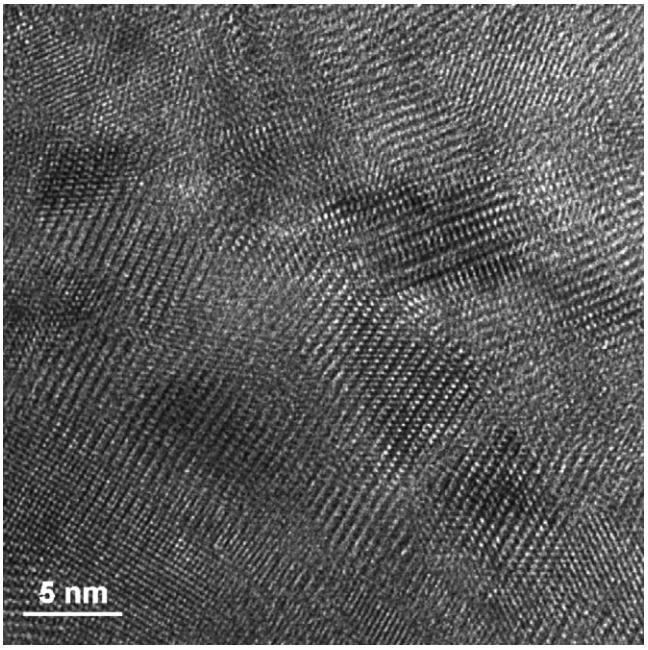

Fig. 10. High-resolution TEM image of plan view foil of sample III as-received; $\langle 11\bar{2}0\rangle$ zone-axis orientation.

Fig. 11 shows HREM images of a top surface foil of the 200 °C heat-treated material. The lower magnification image, Fig. 11a, again clearly shows a domain structure, this time with elongated domains, with aspect ratios of five or more. The scale of the domain microstructures is 2–5 × greater than that in Fig. 10, and adjacent domains appear to have undergone a rotation of 10–30°. (Discussion of the origin of this rotation during heat treatment is deferred to Section 4.) APBs within these elongated rotated domains can be seen in the higher magnification image, Fig. 11b (the white dashed features).

3.3. The ordered structures

In our earlier work [17,18], we suggested a particular motif for the distribution of Mn^{4+} ions and cation vacancies on the basal plane of ε-MnO_2, which is shown in Fig. 12a (we called this structure ε'-MnO_2). (In the representations of the structures in Fig. 12, we show only filled and empty octahedral sites; the hcp oxygen sublattice is not shown.) We further assume, following many authors [1,2,11] and consistent with the notion that [MnO_6] octahedra always avoid face sharing, that perfect ordering exists normal to the basal plane—Mn^{4+} ion, vacant octahedral site, Mn^{4+} ion, vacant octahedral site, etc. The ε' structure represented by the particular distribution of Mn^{4+} ions and vacant sites of Fig. 12a was shown by Balachandran et al. [2] to be very low in energy. However, we used Stadelmeier’s EMS program [26] to simulate electron diffraction patterns of ε'-MnO_2 and found that this structure was not consistent with our electron

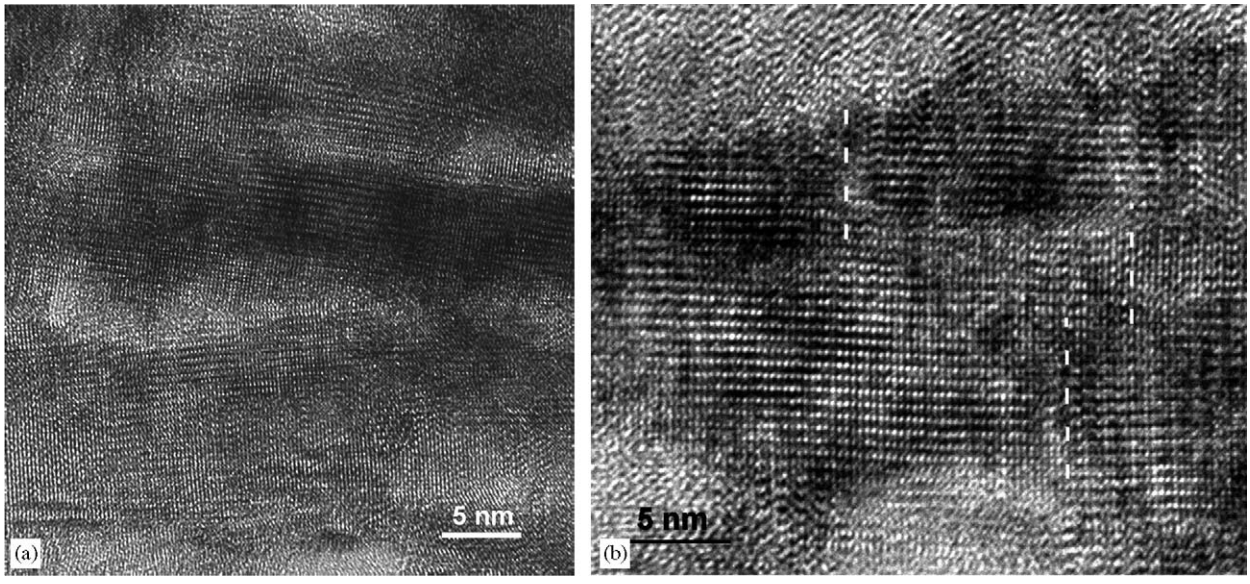

Fig. 11. (a) High-resolution TEM images of sample III after the 1 h 200 °C heat treatment; ⟨110⟩ orientation (ε^{vo}-MnO_2 indices). The white dashed lines in (b) indicate APBs. See text for further discussion.

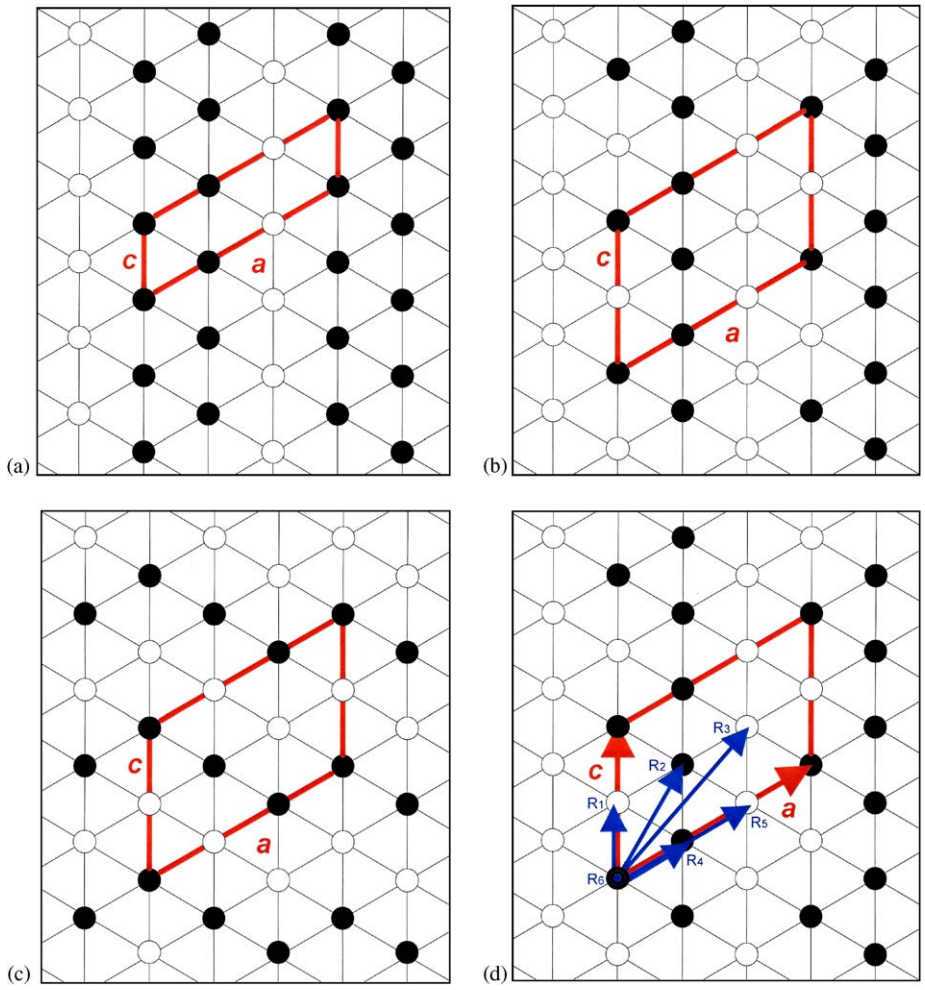

Fig. 12. Structure models for ordered ε-MnO_2 phases: (a) ε′-MnO_2, (b) ε^{vo}-MnO_2, and (c) ε^{bhs}-MnO_2. All structures assume an hcp oxygen sublattice, and show Mn^{4+} ions (filled circles) and structural vacancies (open circles). (d) shows possible **R** vectors for APBs in ε^{vo}-MnO_2.

diffraction data. In particular, while tripling reflections were present in $\langle 11\bar{2}0\rangle$-derived zone-axis diffraction patterns, the doubling reflections present in the experimental $\langle 01\bar{1}1\rangle$- and $\langle 02\bar{2}1\rangle$-derived patterns were not. In spite of its low energy, the structure of Fig. 12a cannot be the structure of ordered ε-MnO_2.

In fact, there are many ways to distribute Mn^{4+} ions and vacant octahedral sites over the octahedral sites of a NiAs-type lattice, while still preserving perfect *c*-axis order. Using a simplified energy model parameterized from Density Functional Theory calculations [2], the energies of thousands of such configurations were calculated by Ceder et al. [27]. We investigated the 20 lowest energy structures found by Ceder et al., and simulated electron diffraction patterns from each. We paid particular attention to those structures that gave rise to doubling and tripling superlattice reflections. Two of particular interest are shown in Figs. 12b and c. The structure implied by the arrangement of Fig. 12b is believed to be the ordered form of ε-MnO_2 formed by heat treatment at 200 °C (henceforth ε^{vo}-MnO_2 for "vacancy ordered"), while that of Fig. 12c is believed to result from heating ε-MnO_2 at 300 °C (henceforth ε^{bhs}-MnO_2 for "broken hexagonal symmetry"). It is interesting to note that the basal planes of ε^{vo}-MnO_2 and ε^{bhs}-MnO_2 are electrically neutral (equal numbers of Mn^{4+} ions and vacant sites), whereas the basal plane of ε′-MnO_2 is not.

Simulated electron diffraction patterns for the model of Fig. 12b are shown in Fig. 13; there is a good match to the ordered electron diffraction patterns shown in Fig. 8, both in regard to the presence of doubling and tripling reflections and to their relative intensity. This ordered structure is monoclinic but pseudohexagonal, space group $P2_1$, with lattice parameters (derived from the XRD pattern of the 198 h/200 °C sample shown in Fig. 3) $a = 0.828$ nm, $b = 0.438$ nm, $c = 0.552$ nm, and $\beta = 60°$. The monoclinic lattice parameters *a*, *b*, and *c* are approximately equal to $\sim 3a_{\varepsilon\text{-}MnO_2}$, $\sim c_{\varepsilon\text{-}MnO_2}$, and $\sim 2a_{\varepsilon\text{-}MnO_2}$, respectively.

Comparable diffraction patterns for a distorted version of the structure of Fig. 12c, ε^{bhs}-MnO_2, are shown in Fig. 14. Different from ε^{vo}-MnO_2, this structure gives rise

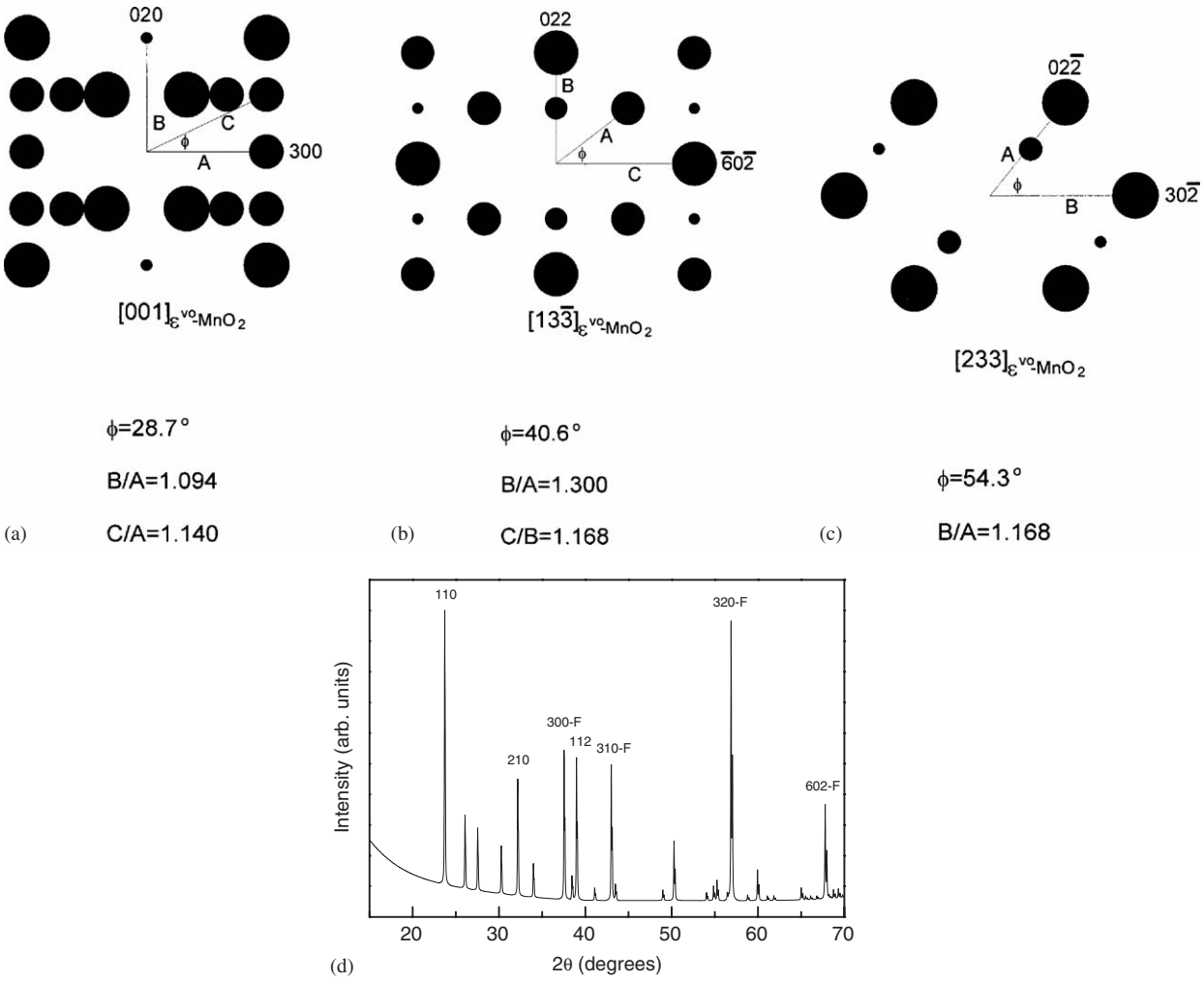

Fig. 13. Simulated electron diffraction patterns of ε^{vo}-MnO_2 in (a) ⟨001⟩, (b) $\langle 13\bar{3}\rangle$, and (c) ⟨233⟩ zone-axis orientations. (d) is a simulated XRD pattern. All diffraction spots peaks in (a)–(c) are indexed according to the structure of ε^{vo}-MnO_2; their diameters are proportional to expected intensities; F in (d) denotes the "fundamental" peaks of disordered ε-MnO_2.

to only strong doubling reflections, including those orientations corresponding to the $\langle 11\bar{2}0\rangle$ zone-axis pattern of disordered ε-MnO_2 (Fig. 14a). These patterns were calculated using the lattice parameters derived from the new reflections in the 300 °C XRD powder pattern shown in Fig. 3, now identified as (111) with $d = 0.356$ nm, (211) with $d = 0.290$ nm, $(\bar{3}02)$ with $d = 0.140$ nm, and (602) with $d = 0.136$ nm, and specifically recognizing the "broken" hexagonal symmetry evident in the microdiffraction pattern of Fig. 9a. The structure is also monoclinic, space group Pc, with $a = 0.811$ nm, $b = 0.437$ nm, $c = 0.541$ nm, and $\beta = 63°$. These lattice parameters are again (nearly) the same simple multiples of the lattice parameters of ε-MnO_2 as was the case for ε^{vo}-MnO_2.

Figs. 13 and 14 also show simulated powder XRD patterns for the structures of ε^{vo}-MnO_2 and ε^{bhs}-MnO_2, calculated using the program RIETAN 2000 [21]. The ε^{vo}-MnO_2 (110), (210), and (112) superlattice reflections in the simulated XRD powder pattern of Fig. 13d are unusually intense and actually correspond to the 1/3 and 2/3 tripling superlattice reflections seen in electron diffraction patterns. In fact, the (110) reflection is as strong as the strongest fundamental reflection in the pattern and occurs at a d spacing of 0.374 nm (23.8° 2θ). We suggest that this very strong (110) reflection in ε^{vo}-MnO_2, has been shifted to an apparent d spacing of ~0.42 nm in as-received sample III, and enormously broadened, due to the very fine domain size. Heat treatment at 200 °C causes domain coarsening and a decrease in apparent d spacing to 0.384 nm. (In other words, the (110) 0.374 nm peak is shifted by a smaller amount in the 200 °C heat-treated material than in the as-received material.) The minor 0.268 nm X-ray peak (33.5° 2θ) in Fig. 3 can now be identified as (210), with $d = 0.278$ (32.2° 2θ) in Fig. 13d. These peak shifts, and the more modest broadening of the fundamental reflections on heat treatment, require further explanation, which we provide in Section 4.

We should also note that some sharpening of this broad (110) reflection would be expected from the domain coarsening. While we believed this has occurred, it is hard to discern in Fig. 3 because of the significant background in this region of the spectrum.

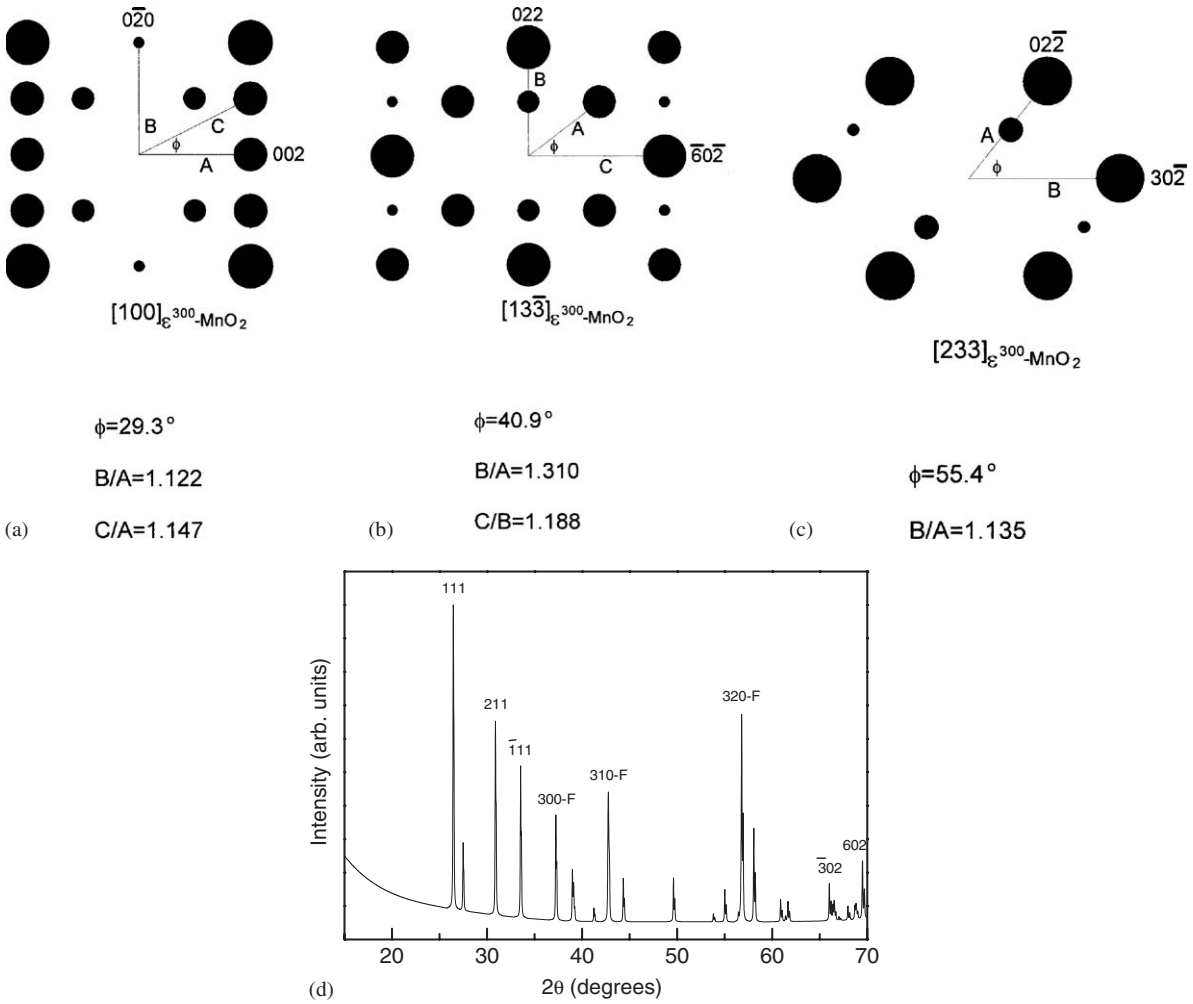

Fig. 14. Simulated electron diffraction patterns of ε^{bhs}-MnO_2 in (a) ⟨100⟩, (b) ⟨13$\bar{3}$⟩, and (c) ⟨233⟩ zone-axis orientations. (d) is a simulated XRD pattern. All peaks are indexed according to the structure of ε^{bhs}-MnO_2; their diameters are proportional to their expected intensities. F in (d) denotes "fundamental" peaks of disordered ε-MnO_2.

The simulated powder XRD pattern of ε^{bhs}-MnO_2 is shown in Fig. 14d. The most intense peak is (111), and is apparently shifted from its simulated 2θ angle of 26.5–25.0° in Fig. 3, whereas (211), ($\bar{3}$02), and (602) appear at 30.8°, 66.8°, and 69.0° 2θ, respectively, compared to their simulated values of 30.9°, 66.1°, and 69.6° 2θ. The fundamental peaks (300), (310), and (320) are within 0.1° of their simulated values of 37.3°, 42.8°, and 56.9°; this is especially significant because the simulation was performed using only the d spacings of (111), (211), ($\bar{3}$02), and (602) and the motif of Fig. 12c. The (111) peak is too spread out and too close to the (211) peak to be visible in the experimental pattern.

4. General discussion

4.1. Nomenclature regarding γ-MnO_2 and the absence of De Wolff defects and microtwins

This combined XRD/TEM/HREM/electron diffraction study has demonstrated that much of the conventional wisdom derived from powder XRD patterns concerning the structure of EMDs may be incorrect—proper analysis requires the use of imaging/diffraction techniques with good spatial resolution, such as TEM and electron diffraction. In particular, most electrochemically active EMDs show the intense but very broad ~0.42 nm peak in XRD patterns; this feature of the XRD characterization has usually been interpreted as arising from defective Ramsdellite, as Ramsdellite has its most intense {110} peak at a d spacing of 0.4057 nm. While the model of Chabre and Pannetier [1] involving De Wolff defects and extensive microtwinning, combined with the XRD simulation program DIFFaX, could simulate aspects of experimental XRD programs, particularly the 0.42 nm XRD peak, our work shows convincingly that this approach does not provide a *unique* description of EMDs. In a similar vein, Hill et al. [28] have used molecular modeling to study the effects of De Wolff disorder, microtwinning, and point defects on EMD XRD patterns. They believed that γ-MnO_2 contained Ramsdellite, pyrolusite, and De Wolff defects and microtwins but were not able to fully and

satisfactorily match simulated with experimental XRD patterns (see Fig. 10 in Ref. [28], for example). Simply put, simulated XRD patterns may be consistent with the presence of such defects but cannot provide *unambiguous* evidence of the presence of such microstructural defects. Our TEM studies would have provided evidence of such defects, *if they had been present in our samples.*

Fig. 1 shows XRD patterns of materials which are largely (sample II) or entirely (sample III) composed of ε-MnO_2; these patterns show the same type of ~0.42 nm peak, albeit with slight shifts in the exact peak angle, as the production material, sample I. The TEM studies of these materials revealed good crystalline material, albeit with very fine crystallites. We strongly suggest that the 0.42 nm peak in XRD patterns arises in materials containing appreciable concentrations of ε-MnO_2 from the strong (110) superlattice reflection of ε^{vo}-MnO_2; the presence of APBs cause the peak broadening and peak shift to a larger and variable *d* spacing.

It is also necessary to discuss Chabre and Pannetier's [1] view on nomenclature of MnO_2 polymorphs. They did not consider ε-MnO_2 as a bona fide phase of MnO_2 and proposed that the name ε-MnO_2 be restricted to samples absent the anomalous 0.42 nm peak, and that the general name γ-MnO_2 be used for samples with a peak corresponding to this *d* spacing. This nomenclature is unsatisfactory, as sample III, which is 100% ε-MnO_2, would be classified as γ-MnO_2 following this definition. A careful review of the EMD literature [1,4–10,12–15] resulted in the scatter plot of Fig. 15, showing the *d* spacing of the anomalous peak for 24 XRD patterns, along with the data of Figs. 1 and 3. It is interesting to note that samples with a *d* spacing of 0.395 nm or below (22.5° 2θ or above) lacked a well-resolved 0.140 nm $\langle 11\bar{2}0 \rangle$ peak, and presumably do not contain any ε-MnO_2. Restricting the term "γ-MnO_2" to such samples might make sense, in that a readily measured criterion—the absence of ε-MnO_2—could be used to define what is meant by γ-MnO_2 in EMDs.

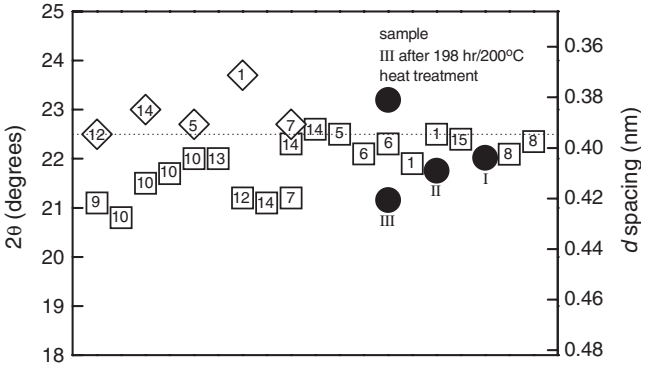

Fig. 15. Scatter plot showing *d* spacings and 2θ values (Cu*K*α radiation) of the broad anomalous peak in EMDs. The numbers inside each datum are the literature references, except for the data of Figs. 1 and 3 (the data for sample III heat treated at 300 °C for 0.5 h is not included). The data represented by the diamonds lacked a well-resolved 0.140 nm peak. See text for further discussion.

Actually, the understanding we have provided of the phase chemistry of EMDs might argue instead that the term γ-MnO_2 be retired altogether. However, Schilling and Dahn [29] have suggested that chemically derived MnO_2 but not EMD, can be considered as an intergrowth of Ramsdellite and pyrolusite domains, i.e., the γ-MnO_2 described by De Wolff [16]. Before this view is accepted, TEM would have to be used to substantiate this claim, as in the present work.

In summary, what is indisputably clear is that ε-MnO_2 is an important component of at least some EMDs, and should be considered in any structural analysis of MnO_2.

4.2. *Ordering and APBs in ε-MnO_2: a new explanation for the anomalous ~0.42 nm peak*

Our work has also shown that heat treatment of disordered ε-MnO_2 results in phase transformations to two new polymorphs of MnO_2, a vacancy-ordered pseudohexagonal structure, ε^{vo}-MnO_2, that forms by ordering of Mn^{4+} cations and structural cation vacancies to the motif shown in Fig. 12b, and a second-ordered structure, ε^{bhs}-MnO_2, whose motif is shown in Fig. 12c, and in which the hexagonal symmetry of the oxygen sublattice common to disordered ε-MnO_2 and ε^{vo}-MnO_2 has been "broken". ε^{vo}-MnO_2 contains "superlattice" reflections that would be absent in disordered ε-MnO_2, and domains of ordered material are present; the sharpness of these superlattice reflections depends on domain size. In the present work, the domains in sample II as-deposited must be relatively large (we did not perform HREM on this sample) and the superlattice reflections in electron microdiffraction patterns are sharp. The domains are much finer in the as-deposited fibrous microstructure of sample III, and sharp superlattice reflections can only be observed when domain coarsening occurs, as happens during the 200 °C heat treatment.

Consider next the origin and crystallographic aspects of the APBs in ε^{vo}-MnO_2 and how they affect XRD patterns. We have demonstrated that Rietveld analysis is not appropriate for EMDs, as there are no provisions for domain size broadening, as opposed to crystallite size broadening, when the domains only broaden certain X-ray reflections, for which $\mathbf{g} \cdot \mathbf{R} \neq 0$ or 1. Here, **g** is a reciprocal lattice vector, and **R** a fault vector characteristic of an APB—the displacement necessary to remove a fault introduced when two domains with different out-of-phase origins impinge.

Imagine a fully disordered form of ε-MnO_2 and a hypothetical ordering transformation. Within the basal plane, half of the available cation sites are randomly occupied by the Mn^{4+} cations, while all columns of filled and vacant cation sites parallel to the *c*-axis are perfectly ordered. Assuming the ordered structure can nucleate at any octahedral site within the basal plane, growth and impingement of ordered domains will give rise to APBs with fault vectors, **R**, equal to 1/3 [100], 1/2 [010], 1/2 [001],

or linear combinations of these. A total of six crystallographically distinct **R** vectors could arise during such an ordering transformation, as shown in Fig. 12d. ($\mathbf{R}_6$ is normal to the basal plane.)

Fault vectors in ordered alloys (or in other compounds which have undergone phase transformations that give rise to equivalent planar defects [23]) are usually determined in TEM experiments by noting the conditions where these planar APBs are not visible in dark-field TEM images. This occurs when $\mathbf{g}\cdot\mathbf{R}=0$ or an integer, where **g** is the reciprocal lattice vector used to form the dark-field TEM image. **R** is usually determined by studying a given region of a TEM thin foil, and forming a series of dark-field images with various **g**'s.

Table 2 is a "truth table" for the reflections of ε^{vo}-MnO_2 present in the 198 h/200 °C XRD pattern shown in Fig. 3. The four strongest "fundamental" reflections of ε^{vo}-MnO_2, corresponding to indices (300), (310), (320), and (602) and 2θ values of 37.5°, 43.0°, 57.0°, and 67.9°, have $\mathbf{g}\cdot\mathbf{R}$ products for most **g**'s and **R**'s of 0 or 1, except for the case of **g** equal to (310) and **R** equal to 1/2[010]. With this one exception, there will be no domain broadening contribution to the X-ray peaks from the fine APBs. However, the domain broadening contribution to the (310) X-ray peak is expected to be modest, as it occurs for only one of the six possible **R** vectors, and the intensity of this reflection in ε^{vo}-MnO_2 has only a small contribution (~20%) from Mn atoms, being dominated by contributions from the oxygen sublattice (this was evident from the RIETAN 2000 simulations).

The occurrence of superlattice reflections as strong as those in Fig. 13d is very unusual. We sympathize with previous researchers who struggled with the interpretations of XRD patterns of the type shown in Fig. 1, absent the knowledge of strong three-dimensional ordering of Mn^{4+} cations and cation vacancies in ε-MnO_2. In fact, Chabre and Pannetier [1] showed, using a numerical simulation, that one-dimensional ordering of Mn^{4+} cations and cation vacancies along the *c*-axis of ε-MnO_2 cannot give rise to the ~0.42 nm peak, but only to a relatively intense diffuse background.

The strong Coulombic repulsion of the Mn^{4+} cations in the NiAs structure is the reason that ordering occurs in ε-MnO_2, and we suspect that disordered ε-MnO_2 rarely forms during electrodeposition. It would be interesting to discern what conditions in the electroplating bath at the electrodeposit/solution interface determine which polymorph of MnO_2 forms, the ε-MnO_2 domain size, whether ε^{vo}-MnO_2 forms in polyphase equiaxed grains, as in samples I and II or as a fibrous structure, as in sample III, etc. Whatever the case, whether superlattice reflections are strong as in sample II and heat-treated ε^{vo}-MnO_2, or diffuse, as in as-deposited sample III, depends only on the domain size. Streaking will occur in electron diffraction patterns when the domain size is of order 10 nm or smaller in characteristic dimensions.

It appears that in such fine domain size materials as the as-deposited sample III, the disorder associated with the APB boundaries is sufficient to cause a lattice expansion from the equilibrium parameters; the 200 °C heat treatment causes the domains to grow and the unit cell to shrink by ~3.8%. The domain rotation that occurs (cf. Figs. 10 and 11) must also be an attempt by the system to minimize electrostatic repulsion of highly charged Mn^{4+} cations, due to their being too closely spaced when they are in the APB boundaries.

Paradoxically, the domain coarsening causes the broad ~0.417 nm peak to sharpen slightly, while the accompanying domain rotation causes the fundamental peaks, e.g., that at 0.140 nm, to broaden. This broadening simply means that the crystallites in the as-received material scatter coherently—the "fundamental" X-rays do not "see" the domains of Fig. 10—whereas in the heat-treated material, the structural features scattering X-rays are the domains of Fig. 11, and the breadth of fundamental peaks reflects the domain size and not the crystallite size. APBs within these domains will cause further broadening of those superlattice reflections for which $\mathbf{g}\cdot\mathbf{R}\neq 0$ or 1.

The shift of the 0.417 nm peak to 0.384 nm during the 200 °C annealing is much more marked than can be explained by lattice compaction or shrinkage, and involves the basic reciprocal lattice geometry of powder XRD

Table 2
"Truth" table for superlattice and "fundamental" reflections in ε^{vo}-MnO_2

2θ angles (deg.)	*d* spacing in nm	**G**	$\mathbf{g}\cdot\mathbf{R}$			Comments
			1/3[100]	1/2[010]	1/2[001]	
23.2	0.384	110	1/3	1/2	0	Streaked
33.5	0.268	210	2/3	1/2	0	Streaked
37.5	0.240	300	1	0	0	Sharp
39.0	0.231[a]	112	1/3	1/2	1	Streaked
43.0	0.210	310	1	1/2	0	Mainly an "oxygen" reflection
57.0	0.161	320	1	1	0	Sharp
67.9	0.138	602	2	0	1	Sharp

[a]This *d* spacing is from an XRD simulation; all other *d* spacings are experimental data.

patterns. A reciprocal lattice description of a powder XRD experiment is shown in Fig. 16. As is conventional, the powder particles are imagined to have their physical origin at the center of the Ewald sphere, whose radius ($1/\lambda$) in reciprocal space is determined by the X-ray wavelength, λ. The origin of the reciprocal lattice of the various particles is at the point where the X-ray beam exits the Ewald sphere. The condition for Bragg diffraction to occur is that a reciprocal lattice vector, $\mathbf{g}_{hkl}$, intersects the Ewald sphere, as shown for particle 1 in Fig. 16; the diffracted beam exits the Ewald sphere at this point. All such intersections and diffracted beams from the ensemble of particles fall on the cone shown in this figure. For coarse particles absent particle size broadening, the diffracted beams are delta functions, and the real space detector records an X-ray peak whose breadth is determined by instrumental effects.

If particle (or domain) size broadening occurs, then a streak or rel-rod is associated with each (otherwise spatially limited) **g** vector, as shown in Fig. 16. The result is that other reciprocal lattice streaks, such as those associated with particles 2 and 3 in Fig. 16, are recorded by the detector as if they were from particle 1. While the obvious result is peak broadening, displacement of the centroid of the peak can also occur if a large collection of particles are considered—because of the curvature of the Ewald sphere, the scattered intensity inside the sphere is denser than outside the sphere. The sense and magnitude of the peak shift depends on the diffraction angle and the shape of the streak in reciprocal space (its orientation, whether it is disk shaped or needle shaped, etc.). Further, the angle between the rel-rod and the **g** vector is constant and depends on the orientation of the planar APB defect. It is then a straightforward (but cumbersome) task to calculate the resulting peak shape—the apparent d spacing (2θ angle) and full-width at half-maximum (FWHM)—for various assumed reciprocal lattice streak shapes. This has been done by Chabre and Pannetier [1] for streaks arising from the supposed De Wolff defects and microtwins in their simulations of "γ-MnO_2" XRD patterns. They showed that peaks shifts could occur that suggest both increasing and decreasing apparent d spacings (and 2θ angles), depending on just such details.

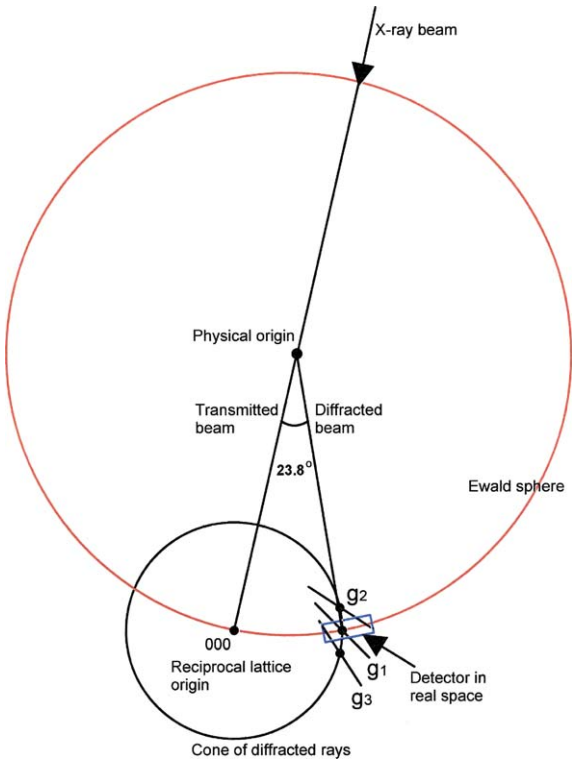

Fig. 16. Reciprocal lattice drawing of powder XRD pattern for sample with "streaked" reflections. See text for further discussion.

In the XRD powder patterns of sample III, the (110) ε^{vo}-MnO_2 peak has shifted from its theoretical position of 23.8° 2θ to 21.3° 2θ in the as-deposited material. Heat treatment at 200 °C has caused domain coarsening and an associated diminution in the streaking of the $\mathbf{g}_{110}$ reciprocal lattice vector. Thus, the peak has sharpened and moved to 23.2° 2θ, but is still shifted from the theoretical valve of 23.8°.

The other intense superlattice reflections in ε^{vo}-MnO_2, (210) and (112), are not visible in the as-received XRD pattern, due to excessive peak broadening. After the 200 °C heat treatment, (210) appears as a discrete reflection at a 2θ value of 33.5°, which can be compared to the theoretical value of 32.2° 2θ. The (112) peak, on the other hand, is too close in d spacing to the (300) and (310) peaks, and too streaked (see Table 2), to appear as a discrete peak, even in the heat-treated material, although it can be seen in electron diffraction patterns (Fig. 8e). The peak shifts of the strong (110) and (210) superlattice reflections occur in opposite senses, which no doubt involves the different values of **g** in the two cases and the exact shape of the reciprocal lattice streaks before and after the 200 °C heat treatment.

The shift of the (111) peak in ε^{bhs}-MnO_2 from the theoretical value of 26.5° 2θ to 25.0° 2θ has a similar explanation, involving the ~10 nm disk-shaped features in Fig. 5d.

One further test of the new model is possible for the ~0.42 nm peak. The intensities of the experimental and simulated XRD patterns of the ordered phases should be simply related. This can be tested for the case of ε^{vo}-MnO_2, which we believe is present in all three materials as-received. These ratios in Fig. 13d for (110):(320) and (110):(602) are approximately 1 and 2.5, respectively. We integrated the area under the ~21° 2θ, ~56° 2θ, and ~67° 2θ peaks in Fig. 1 for samples I, II, and III and found the 21°:56° ratio to be ~1.4, ~1.2 and ~1.5 for samples I, II, and III, respectively, while the 21°:67° ratio was ~5, ~4 and ~6 for these samples. Given the extreme domain broadening, the peak overlap evident in Table 1, and the consequent difficulties of background subtraction, we take these ratios as a reasonable confirmation of the ε^{vo}-MnO_2-based model for the anomalous ~ 0.42 nm peak.

4.3. The energy of the ordered forms of ε-MnO_2

Finally, the issue of the energetics of the ε^{vo}-MnO_2 and ε^{bhs}-MnO_2 structures must be considered. Morgan and Ceder [30] have recently performed first principles calculations (of the type described in Ref. [2]) of the energy of ε^{vo}-MnO_2 and ε^{bhs}-MnO_2 relative to pyrolusite, Ramsdellite, and birnessite (Table 3). These 0 K calculations confirmed that pyrolusite is the ground-state structure, but that Ramsdellite and ε^{bhs}-MnO_2 are nearly as stable and nearly equal in energy, with ε^{vo}-MnO_2 being only 53 meV less stable than pyrolusite.

However, the earlier theoretical work [2] demonstrated that the presence of Ruetschi defects can change the relative energetics of the MnO_2 polymorphs, and Table 3 shows that Ruetschi defects are particularly potent in stabilizing ε^{vo}-MnO_2. The new calculations show that in the presence of 13% Ruetschi defects, a concentration thought to be typical of EMDs, Ramsdellite, ε^{bhs}-MnO_2 and ε^{vo}-MnO_2 are all more stable than pyrolusite. Furthermore, the differences in energy between these three defective MnO_2 polymorphs are so small that the phase chemistry of any particular EMD cannot be predicted with certainty, but will depend on the concentration of Ruetschi defects, possible defect interactions in highly defective MnO_2, which have not been modeled, and poorly understood details of the electrodeposition. However, we would argue that the likelihood of forming ε^{vo}-MnO_2 during electrodeposition increases with an increasing Ruetschi defect concentration, given the potent effect of Ruetschi defects on stabilizing ε^{vo}-MnO_2 (Table 3).

That ε^{bhs}-MnO_2 rather than Ramsdellite or pyrolusite forms from ordered ε^{vo}-MnO_2 on heating to 300 °C is easily understood from the recognition that the structural changes between ε^{vo}-MnO_2 and ε^{bhs}-MnO_2 are more modest than those between ε^{vo}-MnO_2 and Ramsdellite, and the energy difference between defect-free Ramsdellite and defect-free ε^{bhs}-MnO_2 is very small (Table 3). (Significant annealing of point defects could well occur at 300 °C so we need to compare the energetics of defect-free material.)

Table 3
Paramagnetic energetics of MnO_2 polymorphs [30]

	Lattice energy relative to pyrolusite (meV)	Isolated Ruetschi defect energy/defect (meV) relative to birnessite	Lattice energy (relative to pyrolusite); all polymorphs contain 13% Ruetschi defects (meV)
Birnessite	115	237	146
Ramsdellite	6	−382	−43
ε^{vo}-MnO_2	53	−579	−22
ε^{bhs}-MnO_2	10	−298	−29
Pyrolusite	0	−397	0

5. Conclusions

Electrolytic manganese dioxides (EMDs) contain structure at two length scales. In some of the materials we studied, the EMD is polyphase, containing principally Ramsdellite and ε-MnO_2, in which case the length scales are those that characterize single-phase ellipsoidal crystallites, with characteristic dimensions of some tens of nanometer, and polyphase equiaxed grains, 0.1–0.2 μm in diameter.

Alternatively, the EMDs can be fibrous and single-phase ε-MnO_2. The fibers are some microns in length, with cross-sectional dimensions some tens of nanometer in characteristic dimensions; the fibers are textured, with a strong $\langle 11\bar{2}0\rangle$ orientation and are made up of stacks of ~15 nm thick crystallites. It is not known what conditions during electrodeposition determine the resulting microstructure and phase chemistry.

ε-MnO_2 generally forms in an ordered structure, ε^{vo}-MnO_2; it is monoclinic but pseudohexagonal, space group $P2_1$, with lattice parameters $a = 0.828$ nm, $b = 0.438$ nm, $c = 0.552$ nm, and $\beta = 60°$. Ordered ε^{vo}-MnO_2 contain domains separated by APBs, which cause broadening and peak shifts of unusually intense superlattice reflections. This strongest such reflection is (110), $d = 0.374$ nm (23.8° 2θ, Cu$K\alpha$ radiation). The peak can shift to ~21° 2θ in those ε-MnO_2-containing materials with an unusually fine domain size; in such materials, this "anomalous" peak is not due to defective Ramsdellite, as has previously been suggested.

Heat treating ε-MnO_2 at 300 °C leads to a second-ordered structure, ε^{bhs}-MnO_2, in which the hexagonal symmetry of ε-MnO_2 and ε^{vo}-MnO_2 has been broken; it is also monoclinic, space group Pc, $a = 0.811$ nm, $b = 0.437$ nm, $c = 0.541$ nm, and $\beta = 63°$.

The theoretical calculations recently conducted by Morgan and Ceder [30] make clear that ε^{vo}-MnO_2 is significantly stabilized by Ruetschi defects—Mn vacancies charge compensated by four protons (in the form of OH^- ions)—and has a comparable energy to Ramsdellite in defective EMDs.

Finally, we have demonstrated that conventional powder XRD is limited in its use for phase identification of EMDs, and have suggested that if the EMD community continues to use the term "γ-MnO_2", it should be restricted to materials that do not contain ε-MnO_2.

Appendix A. Rietveld analysis

The Rietveld program refines the following parameters: (i) unit cell lattice parameters, which are related to the peak positions; (ii) the atomic positions and temperature parameters, which are related to the integrated peak intensities; (iii) parameters of the peak profile function, which are related to the FWHM of the peaks; and (iv) scale factors for these (assumed) multi-phase materials, which are related to the mass fraction of each polymorph. The

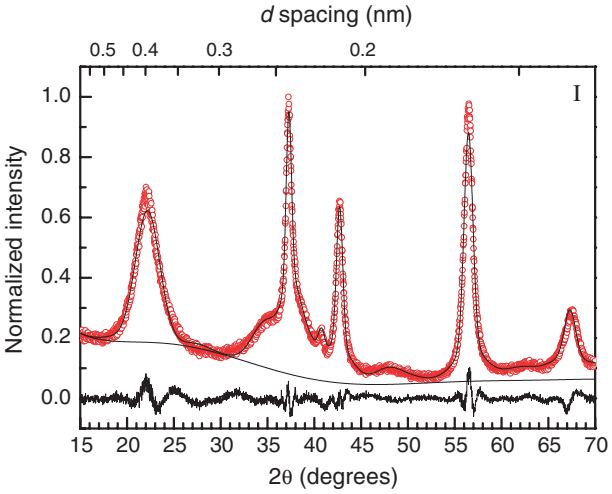

Fig. A.1. XRD pattern of sample I (circles) and its Rietveld fit. The Rietveld analysis suggests a phase content of 51% ε-MnO_2, 44% Ramsdellite, and 5% pyrolusite.

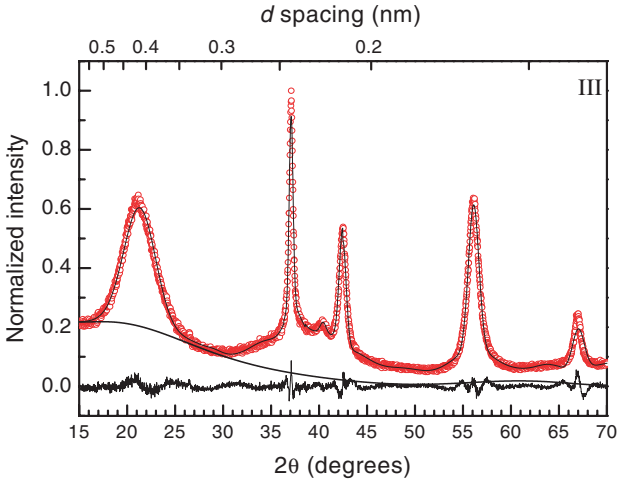

Fig. A.3. XRD pattern of sample III (circles) and its Rietveld fit. The Rietveld analysis suggests a phase content of 44% ε-MnO_2, 50% Ramsdellite, and 6% pyrolusite.

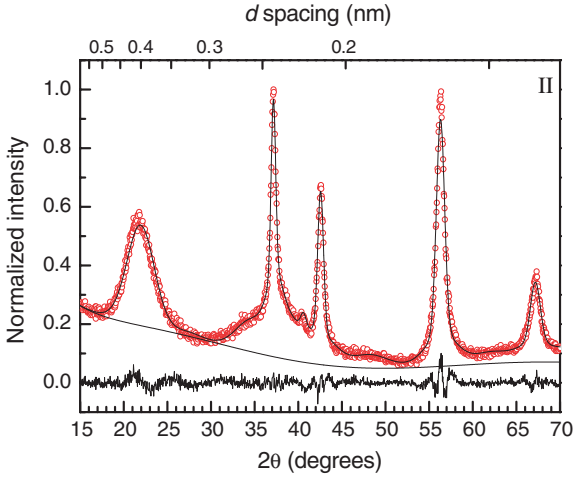

Fig. A.2. XRD pattern of sample II (circles) and its Rietveld fit. The Rietveld analysis suggests a phase content of 47% ε-MnO_2, 44% Ramsdellite, and 9% pyrolusite.

FWHMs are calculated from the refined parameters of the peak profile function (a pseudo-Voigt function, which is defined as a mixed Gaussian/Lorenzian) and the particle size and strain of each polymorph are calculated using the following formula:

$$\beta \cos\theta = 2\eta \sin\theta + \lambda/D, \quad \text{(A.1)}$$

where β and θ are the FWHM (in radians) and Bragg angle of each peak in the diffraction pattern, η is the strain, λ the X-ray wavelength, and D the particle size. This formula is based on early work by Scherrer, Stokes and Wilson [31,32] and Williamson and Hall [33].

The quality of the XRD powder patterns of samples I, II, and III was not good enough to refine the lattice parameters of the multi-phase assemblage. Instead, we used the lattice parameters from Table 1 to determine the mass fraction of each phase, assuming the Ramsdellite pyrolusite, and ε-MnO_2 were the only phases present.

Rietveld analysis also yields statistical parameters, R_{wp} and R_e, that define the goodness of fit of the analysis. They are defined as follows: R_{wp} is the conventional crystallographic goodness-of-fit R parameter, with appropriate weighting given to the intensity of each peak. R_e is the minimum value of R_{wp}, estimated statistically. If $s = R_{wp}/R_e$ is less than 1.3, the fit is considered to be a good one.

Figs. A.1–A.3 show the data from Fig. 1 and the Rietveld fits. As is usual, the curve at the bottom of each figure shows the difference between the data and the simulation.

Appendix B. Ion-beam-induced phase transformation

If no precautions are taken, ion-beam thinning can induce the transformation of ε-MnO_2 to a spinel form of MnO_2 (λ-MnO_2) during TEM thin foil preparation. The TEM foils used in this work were prepared using two different ion-beam thinning apparatuses: a Gatan "Duo-Mill" with a liquid nitrogen-cooled specimen stage and a Gatan precision ion polishing system (PIPS). The PIPS apparatus generates a well-focused ion beam with a higher beam current than is present in the DuoMill. The microstructures of the TEM foils from the fibrous specimen III were the same using both thinners, but they showed different electron diffraction patterns. Foils made with the PIPS instrument showed diffraction patterns of λ-MnO_2 (Fig. B.1), whereas no spinel was found in microdiffraction patterns of foils made using the cooling stage in the DuoMill (Fig. 7b). The $\varepsilon \rightarrow \lambda$ transformation is obviously a thin foil artifact that occurs when TEM foils are made in the PIPS ion thinner. Use of a liquid N_2-cooled stage eliminated this artifact almost completely, although

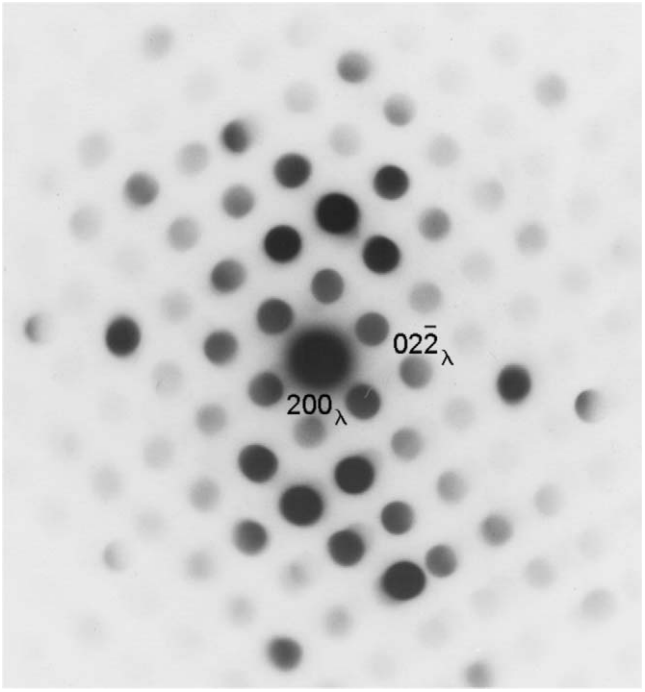

Fig. B.1. Electron microdiffraction pattern of a crystallite in a plan view foil of as-received sample III, showing γ-MnO_2 in a $\langle 011 \rangle$ orientation. This sample had been prepared in a Gatan PIPS Ion Thinner, without liquid N_2 cooling.

some minimal $\varepsilon \rightarrow \lambda$ transformation could occasionally be found in the thinnest regions of electron transparent foils.

The oxygen sublattice of the NiAs structure of disordered ε-MnO_2 involves perfect hcp stacking of oxygen, with Mn ions occupying half of the octahedral positions. The spinel structure of λ-MnO_2 involves oxygen in fcc stacking, with Mn occupying all the 16*d* octahedral sites, the 8*a* tetrahedral sites in the spinel structure (A in the formula AB_2O_4) being vacant. However, the exact mechanism by which the hcp oxygen sublattice transforms to an fcc form is not clear, given that ion thinning of oxides for TEM foil preparation is not thought to involve excessive heating.

Appendix C. Ambiguity in electron microdiffraction patterns

As is clear from the main text, the principal phases of MnO_2 in EMDs are Ramsdellite, pyrolusite, and disordered and ordered versions of ε-MnO_2. All these polymorphs have Mn ions in octahedral coordination in an oxygen sublattice, which, in disordered ε-MnO_2 and ε^{vo}-MnO_2, occupy a perfect hcp lattice. In Ramsdellite, the oxygen sublattice forms a distorted hcp array, while the oxygen sublattice in pyrolusite is even further distorted from hcp stacking. The crystallographic data for these phases are included in Table 1, except for ε^{vo}-MnO_2, for which $a = 0.828\,\text{nm}$, $b = 0.438\,\text{nm}$, $c = 0.552\,\text{nm}$, $\beta = 60^\circ$, and space group $P2_1$, and ε^{bhs}-MnO_2, for which $a = 0.811\,\text{nm}$, $b = 0.437\,\text{nm}$, $c = 0.541\,\text{nm}$, $\beta = 63^\circ$, and space group Pc.

The five phases of interest have similar oxygen sublattices but different distributions of manganese cations, and electron diffraction patterns of certain zone-axis orientations can appear very similar. The most important issue in solving any electron diffraction pattern is to identify the crystallite orientation and phase, and the most reliable data are the interplanar angles between two sets of diffraction spots. (The *d* spacings calculated from the pattern are not reliable because of the uncertainties in the camera length of the microscope used for any diffraction pattern.) In some cases, however, there exists ambiguity in the phase identification, because small differences in interplanar angles can be larger than the experimental uncertainty. Fig. C.1 shows simulated electron diffraction patterns of disordered ε-MnO_2 in a $\langle 2\bar{1}\bar{1}0 \rangle$ zone-axis orientation, Ramsdellite in a $\langle 012 \rangle$ zone-axis orientation, and ε^{vo}-MnO_2 in a $\langle 203 \rangle$ zone-axis orientation. The difference between Ramsdellite, and ordered and disordered ε-MnO_2 in the indicated Φ angle is only 0.3° or 0.4°, so it is not possible to distinguish these polymorphs in this orientation. (Our measurement accuracy is $\sim 0.5^\circ$.)

This is the most difficult orientation as far as ambiguity is concerned. Normally, one would tilt the foil to a zone axis for which unambiguous interpretation is possible, but the small crystallite size of EMD precludes this strategy. Note, however, that the presence of the doubling and tripling superlattice reflections in other zone-axis orientations uniquely identify ε^{vo}-MnO_2 and ε^{bhs}-MnO_2.

Fig. C.2 shows an example of possible ambiguity between ε^{vo}-MnO_2 and Ramsdellite. In this case, however, the difference of interplanar angles is sufficiently large (0.9°) that with well-focused diffraction patterns, it should be possible to differentiate between the two polymorphs.

This ambiguity between Ramsdellite and disordered ε-MnO_2 (or ε^{vo}-MnO_2) diffraction patterns is of importance, especially because of the debate between proponents of a single-phase defective Ramsdellite models for EMDs [1,4], and the polyphase model for non-fibrous EMDs advocated here. For example, Bowden et al. [4] interpreted their streaked electron diffraction patterns as arising from Ramsdellite containing linear defects. However, a distinction between Ramsdellite and ε-MnO_2 based on electron diffraction data must take the ambiguity of diffraction patterns just discussed into account, since as already noted, the accuracy in measuring diffraction angles is no better than $\sim 0.5^\circ$. The diffraction patterns included in the paper by Bowden et al. are precisely the orientations showing ambiguity. Considering just the Φ angles in their published diffraction patterns, it appears that Fig. 5a in their paper is of a Ramsdellite region, Fig. 5b is ambiguous, given the possible 0.5° angular error, and Fig. 5c is too poorly focused to distinguish between Ramsdellite and ordered ε^{vo}-MnO_2.

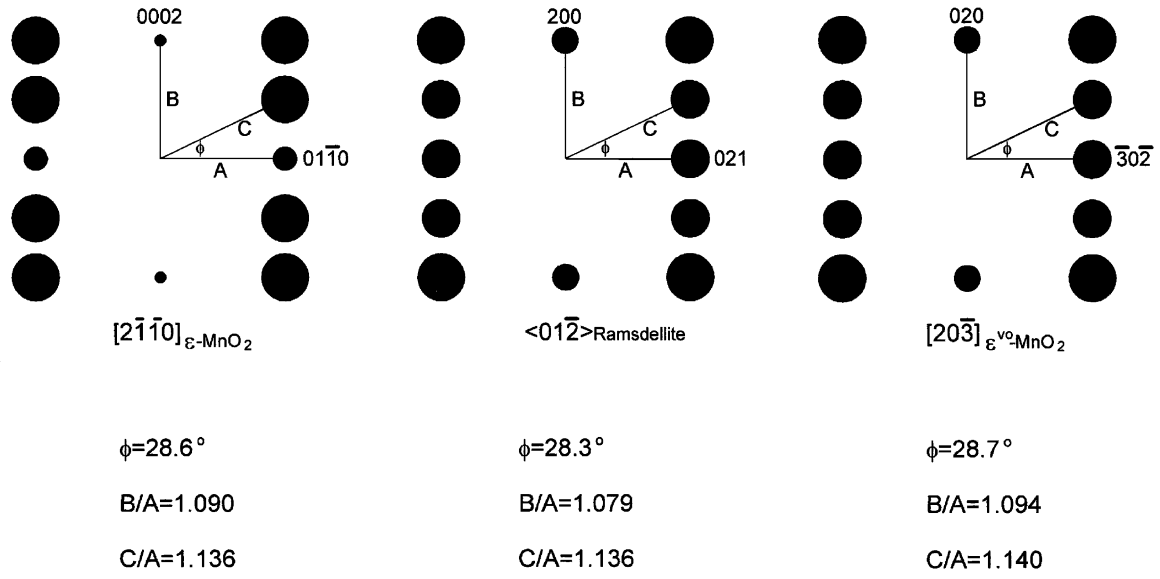

Fig. C.1. Simulated electron diffraction patterns for disordered ε-MnO_2 in a $\langle 2\bar{1}\bar{1}0\rangle$ zone-axis orientation, for Ramsdellite in a $\langle 01\bar{2}\rangle$ zone-axis orientation, and for ε^{vo}-MnO_2 in a $\langle 20\bar{3}\rangle$ zone-axis orientation.

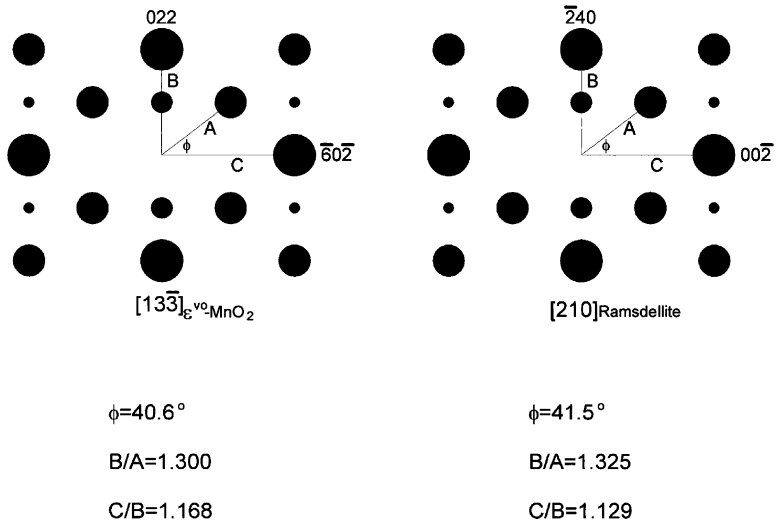

Fig. C.2. Simulated electron diffraction patterns of ε^{vo}-MnO_2 in a $\langle 13\bar{3}\rangle$ zone-axis orientation and Ramsdellite in a $\langle 210\rangle$ zone-axis orientation.

References

[1] Y. Chabre, J. Pannetier, Prog. Solid State Chem. 23 (1995) 1.
[2] D. Balachandran, D. Morgan, G. Ceder, J. Solid State Chem. 166 (2002) 91.
[3] D. Balachandran, D. Morgan, G. Ceder, A. van de Walle, J. Solid State Chem. 173 (2003) 462.
[4] W. Bowden, R. Sirotina, S. Hackney, ITE Lett. 4 (1) (2003) B1.
[5] T.N. Andersen, Prog. Batteries Battery Mater. 11 (1992) 105.
[6] R. Williams, R. Fredlein, G. Lawrance, D. Swinkels, C. Ward, Prog. Batteries Battery Mater. 13 (1994) 102.
[7] C.J. Poinsignon, Mater. Res. Soc. Symp. Proc. 548 (1999) 261.
[8] W. Bowden, ITE Lett. 1 (6) (2000) 903.
[9] F. Freund, E. Könen, E. Preisler, in: A. Kozawa, R.J. Brodd (Eds.), Manganese Dioxide Symposium, Cleveland, vol. 1, 1975, p. 328.
[10] E. Preisler, J. Appl. Electrochem. 6 (1976) 301.
[11] [a] Y.D. Kondrashev, A.I. Zaslavsky, Isv. Akad. Nauk. SSSR Ser. Siz. 15 (1951) 179;
[b] P.M. De Wolff, J.W. Visser, R. Giovanoli, R. Brutsch, Chimia 32 (7) (1978) 257.
[12] E. Preisler, in: Second Battery Market Symposium, 1985, p. 247.
[13] W.C. Maskell, Electrochem. Acta 26 (1981) 1403.
[14] E. Preisler, J. Appl. Electrochem. 19 (1989) 540.
[15] D. Mazza, S. Ronchetti, S. Bodoardo, M. Lucco-Borlera, Mater. Sci. Forum 630 (1998) 278–281.
[16] P.M. De Wolff, Acta Crystallogr. 12 (1959) 341.
[17] A.H. Heuer, A.Q. He, P.J. Hughes, F.H. Feddrix, ITE Lett. 1 (6) (2000) B50.
[18] A.H. Heuer, C.H. Kim, L.C. Zhang, A.Q. He, Proc. Seventh Int. Symp. Adv. Phys. Fields 92 (2001).
[19] D.E. Simon, T.N. Andersen, C.D. Elliott, ITE Lett. 1 (3) (2000) B1.
[20] P. Ruetschi, J. Electrochem. Soc. 131 (1984) 2737.

[21] F. Izumi, T. Ikeda, Mater. Sci. Forum 198 (2000) 321–324.
[22] J.C. Charenton, P. Strobel, J. Solid State Chem. 77 (1988) 33.
[23] A.H. Heuer, G.L. Nord Jr., Polymorphic phase transformations, in: H.R. Wenk, P.E. Champness, J.M. Christie, J.M. Cowley, A.H. Heuer, G. Thomas, N.J. Tighe (Eds.), Electron Microscopy in Mineralogy, Springer, New York, 1976.
[24] A. Loiseau, A. Lasalmonie, G. Van Tendeloo, J. Van Landuyt, S. Amelinckx, Acta Cryst. B 41 (1985) 411.
[25] P. Hirsch, A. Howie, R. Nicholson, D. Pashley, M. Whelan, Electron Microscopy of Thin Crystals, Robert Krieger Publishing Co, New York, 1977.
[26] EMS On Line, http://cimesg1.epfl.ch/CIOLS/crystal1.pl.
[27] G. Ceder, D. Morgan, D. Balachandran, private communication, 2004.
[28] J.R. Hill, C.M. Freeman, M.H. Rossouw, J. Solid State Chem. 177 (2004) 165.
[29] O. Schilling, J.R. Dahn, J Appl. Crystallogr. 31 (1998) 396.
[30] D. Morgan, G. Ceder, private communication, 2004
[31] A.R. Stokes, A.J.C. Wilson, Proc. Cambridge Philos. Soc. 38 (1942) 313.
[32] A.R. Stokes, A.J.C. Wilson, Proc. Cambridge Philos. Soc. 40 (1944) 197.
[33] G.K. Williamson, W.H. Hall, Acta Metall. 1 (1953) 122–131.